Published in final edited form as:
J Comput Neurosci. 2007 October ; 23(2): 143–168. doi:10.1007/s10827-007-0024-z.

Somato-dendritic mechanisms underlying the electrophysiological properties of hypothalamic magnocellular neuroendocrine cells: A multicompartmental model study

Alexander O. Komendantov,
Center for Computational Science, Tulane University, New Orleans, LA 70118, USA. Department of Neurobiology and Anatomy, Drexel University College of Medicine, 2900 Queen Lane, Philadelphia, PA 19129, USA

Natalia A. Trayanova, and
Center for Computational Science, Tulane University, New Orleans, LA 70118, USA. Department of Biomedical Engineering, Johns Hopkins University, Baltimore, MD 21218, USA

Jeffrey G. Tasker
Center for Computational Science, Tulane University, New Orleans, LA 70118, USA. Division of Neurobiology, Department of Cell and Molecular Biology, Tulane University, New Orleans, LA 70118, USA. Neuroscience Program, Tulane University, New Orleans, LA 70118, USA

Alexander O. Komendantov: komendantov@drexel.edu

Abstract

Magnocellular neuroendocrine cells (MNCs) of the hypothalamus synthesize the neurohormones vasopressin and oxytocin, which are released into the blood and exert a wide spectrum of actions, including the regulation of cardiovascular and reproductive functions. Vasopressin-and oxytocin-secreting neurons have similar morphological structure and electrophysiological characteristics. A realistic multicompartmental model of a MNC with a bipolar branching structure was developed and calibrated based on morphological and in vitro electrophysiological data in order to explore the roles of ion currents and intracellular calcium dynamics in the intrinsic electrical MNC properties. The model was used to determine the likely distributions of ion conductances in morphologically distinct parts of the MNCs: soma, primary dendrites and secondary dendrites. While reproducing the general electrophysiological features of MNCs, the model demonstrates that the differential spatial distributions of ion channels influence the functional expression of MNC properties, and reveals the potential importance of dendritic conductances in these properties.

Keywords

Hypothalamic neuron; Oxytocin; Vasopressin; Dendritic conductance; Multicompartmental model

1 Introduction

Magnocellular neuroendocrine cells (MNCs) of the hypothalamic paraventricular nucleus (PVN) and supraoptic nucleus (SON) synthesize the neurohormones vasopressin (VP) or oxytocin (OT), which are released from the neurohypophysis into the blood and exert a wide

Correspondence to: Alexander O. Komendantov, komendantov@drexel.edu.
Action Editor: Eric De Schutter

spectrum of actions, including regulation of cardiovascular, reproductive and homeostatic functions. Magnocellular neurons show specific electrophysiological properties and bursting patterns that distinguish them from other neurons of the central nervous system. Among the most distinctive properties of MNCs is their capacity to generate repetitive bursts of action potentials (Poulain and Wakerley 1982). OT-secreting cells demonstrate brief (2–4 s), synchronized high-frequency bursts (40–80 Hz) during reflex milk ejections (Wakerley and Lincoln 1973). VP-secreting cells respond to changes in blood pressure and blood osmolality with a phasic firing pattern, or asynchronous, lower-frequency bursts (8–15 Hz) lasting tens of seconds and separated by silent intervals of similar durations (Brimble and Dyball 1977; Poulain et al. 1977; Poulain and Wakerley 1982).

Oxytocin- and VP-secreting MNCs are quite similar to one another with respect to their ontogenic, morphological and membrane electrical properties. Several voltage- and Ca^{2+}-activated currents are known to contribute to the electrogenic properties of both OT and VP MNCs, including K^+, Na^+, Ca^{2+} and non-selective cationic currents (Hatton and Li 1998). Differences in electrophysiological properties between OT-secreting and VP-secreting cells are relatively few and subtle, and include differences in depolarizing after potentials (DAPs), which are more prevalent in, but not exclusive to, VP-secreting cells (Stern and Armstrong 1996); in a sustained outward rectification, found only in OT-secreting cells (Stern and Armstrong 1995; Armstrong and Stern 1997); in an A current-mediated transient outward rectification, which is more pronounced in VP-secreting cells (Stern and Armstrong 1996; Fisher et al. 1998); and in a time-dependent inward rectification, more prominent in OT-secreting cells than in VP-secreting cells (Hirasawa et al. 2003). Nevertheless, the electrophysiological properties of OT- and VP-secreting MNCs are, for the most part, remarkably similar, and they have been used routinely as a fingerprint to distinguish MNCs as a group from other hypothalamic neurons (Hoffman et al. 1991; Tasker and Dudek 1991; Stern and Armstrong 1997).

Experimental data on the differential distribution of ion channels between soma and dendrites have been obtained in other types of neurons (Golding and Spruston 1998; Larkum et al. 1996; Magee and Johnston 1995; Stuart and Sakmann 1994; for review see Migliore and Shepherd 2002), but direct recordings from the dendrites of magnocellular neurons have not been performed to date. It is not known, therefore, what impact the distribution of ionic conductances between the soma and dendrites has on the electrophysiological properties of MNCs. The development of a multicompartmental model of MNCs will allow predictions to be made concerning the role of spatially distributed ion channels in the distinctive electrophysiological properties of these cells under different physiological conditions. Therefore, we have constructed a multicompartmental model based on the Hodgkin-Huxley formalism and Ca^{2+} dynamics that reproduces the basic electrophysiological properties of MNCs. The model has a simplified but morphologically realistic structure and biophysical parameters. Using this model, we demonstrate how the compartmental distribution of conductances underlying voltage- and Ca^{2+}-dependent currents and intracellular Ca^{2+} dynamics may contribute to the electrophysiological properties of MNCs. Some of these findings have appeared in abstract form (Komendantov et al. 2002, 2003).

2 Materials and methods

2.1 Model development

2.1.1 Morphological structure and electrotonic properties of the model—Under unstimulated conditions, the MNCs have a relatively simple morphology that is similar for both OT and VP neurons (Stern and Armstrong 1998). According to morphometric analyses of identified OT and VP neurons in the SON (Stern and Armstrong 1998), the soma of OT neurons of diestrous female rats has long axis of 25.7±1.3 μm and a short axis of 15.9±1.1

μm, and the soma of VP neurons has a long axis of 24.6±1.8 μm and a short axis of 15.9± 1.2 μm. Both cell types show a relatively symmetric branching pattern. The dendritic diameter decreases with increasing branch order from 2 μm in the first order branches to 1.5–1 μm in the second order and higher branches. Total length of terminal branches of MNCs is about 800–1,000 μm. Maximal extension of the dendritic trees for VP neurons of diestrous rats is 268±28.3 μm and for OT neurons is 316±32.9 μm rats (Stern and Armstrong 1998). Our multicompartmental model of the hypothalamic MNC includes a soma and two double branching dendrites subdivided into primary and secondary compartments (Fig. 1). The soma was modeled as a cylinder, 15 μm in diameter and 25 μm in length. The primary and secondary dendrites were also modeled as cylinders, 2.0and 1.0 μm in diameter and 50 and 200 μm in length, respectively (see Appendix). This symmetrical dendritic structure of the model was selected for its computational simplicity while retaining a similarity with the morphometric structure of hypothalamic MNCs (Armstrong 1995; Millhouse 1979; Stern and Armstrong 1998). The model equations and parameters are presented in the Appendix and in the Table 1; these were maintained constant between simulated protocols unless otherwise specified.

Each compartment of the model includes a leak current (I_L) as a sum of leaks for Na^+ and K^+ ($I_{L,Na}$ and $I_{L,K}$). The description of intercompartmental currents is similar to that used in previous models of midbrain dopaminergic neurons (Canavier 1999; Komendantov and Canavier 2002; Komendantov et al. 2004). The model, with its secondary branching structure and realistic sizes of compartments, has a surface area that approximates the surface area of real MNCs (Stern and Armstrong 1998), which allowed the use of a realistic value of the specific capacitance (C_m =1 μF/cm^2). Using leak currents, the input resistance (R_i =976 MΩ), the time constant (54 ms) and the resting membrane potential (−58 mV) were adjusted to match data obtained in *in vitro* brain slice experiments on magnocellular neurons using patch electrodes (Luther and Tasker 2000). Thus this simplified model with cylindrical compartments maintains a general correspondence between its morphological and electrophysiological properties and those of real hypothalamic neurons (Armstrong 1995; Chevaleyre et al. 2001; Luther and Tasker 2000; Randle et al. 1986; Stern and Armstrong 1998).

2.1.2 Voltage-gated and Ca^{2+}-activated membrane currents—As illustrated in Fig. 1, the model contains several voltage-gated currents: the transient voltage-gated sodium current (I_{Na}) (Tanaka et al. 1999), the delayed rectifier potassium current ($I_{K(DR)}$) (Luther and Tasker 2000), the A-type transient potassium current (I_A) (Luther and Tasker 2000), and L- and N-type Ca^{2+} currents ($I_{Ca,L}$, $I_{Ca,N}$) (Foehring and Armstrong 1996;Joux et al. 2001). It also contains the following Ca^{2+}-dependent currents: a K^+ current mediated by large conductance K^+ (BK) channels (Dopico et al. 1999), a K^+ current mediated by small conductance K^+ (SK) channels (Kirkpatrick and Bourque 1996), a non-selective cation (CAN) current (I_{CAN}) (Ghamari-Langroudi and Bourque 2002), and a slowly activated K^+ current in OT neurons (Stern and Armstrong 1995,1997).

The voltage-gated and Ca^{2+}-dependent currents have the following standard generic forms for inactivating currents and non-inactivating currents, respectively:

$$I_\kappa = g_\kappa \alpha^\beta \gamma^\delta (V - E_\kappa) \text{ or}$$
$$I_\kappa = g_\kappa \alpha^\beta (V - E_\kappa)$$

where I_κ is a current, g_κ is a conductance, E_κ is a reversal potential, α is an activation, and γ is an inactivation. For all voltage-gated currents (I_{Na}, $I_{K(DR)}$, I_A, $I_{Ca,L}$, $I_{Ca,N}$, I_{SOR}), dynamics of activation and inactivation X was described by the equation:

$$dX/dt=(X_\infty(V) - X)/\tau_x,$$

where $X_\infty(V)$ is the steady-state activation/inactivation and τ_X is the time constant. The steady-state activation and inactivation of the voltage-gated currents were described by Boltzmann functions:

$$X_\infty(V)=1.0/[\,1.0+\exp[\,-(V - V_{\mathrm{half},x})/\theta_x\,]],$$

where $V_{\mathrm{half},x}$ is the half activation voltage for the gating variable X and θ_x is the slope factor for that variable.

Distributions of active conductances between compartments were based on direct experimental data and indirect evidence from different types of neurons reported in the literature (Bischofberger and Jonas 1997; Hoffman et al. 1997; Joux et al. 2001; Mainen and Sejnowski 1999; Migliore and Shepherd 2002). Parameters for the time constants and conductances of I_{Na}, I_A, and I_{BK} were adjusted in order to fit the shape, amplitude, and duration of the action potentials in the model to experimental data from rat MNCs (Greffrath et al. 2004; Luther and Tasker 2000; Stern and Armstrong 1996; Tasker and Dudek 1991; Teruyama and Armstrong 2002).

Na^{+} and K^{+} voltage-gated currents: Activation parameters in the Hodgkin-Huxley type equations for I_{Na} and $I_{K(DR)}$ were raised to the power of three (m^3 and n^3, respectively) and the I_A activation parameter was raised to the power of four (p^4) (see Appendix). For model simplicity, we used the steady state value of activation for the sodium current (m_∞), because we focused on the electrophysiological processes, which are much longer than single spike rising phase. The function for the time constant of inactivation (τ_h) of this current was selected as the sum of two Boltzmann functions in order to satisfy the dynamics of the sodium current in voltage clamp experiments in freshly isolated SON neurons (Tanaka et al. 1999). The function for the time constant of inactivation of the potassium current (τ_n) was selected as the sum of three Boltzmann functions in order to provide correspondence of spike shape and duration. The structure of the model provides a good fit to published results from voltage-clamp experiments (Luther and Tasker 2000;Tanaka et al. 1999) and produces spikes with amplitude and duration similar to those observed in MNCs. Steady-state activation and inactivation characteristics of I_{Na}, $I_{K(DR)}$ and I_A are presented in Fig. 2(a).

Ca^{2+}-activated K^{+} currents: The model includes two Ca^{2+}-activated K^{+} currents mediated by SK and BK channels (Marty 1981; Marty and Neher 1985; Vergara et al. 1998). Activation of the SK channels is voltage independent and highly sensitive to intracellular Ca^{2+} (Hille 2001; Sah and Davies 2000); BK channel activation is both voltage-and Ca^{2+}-dependent (Vergara et al. 1998; Dopico et al. 1999). While activation of BK channels contributes to the falling phase of individual action potentials and the generation of the fast after hyperpolarizing potential (AHP) or hyperpolarizing after potential in many types of neurons (Lancaster and Adams 1986; Lancaster and Nicoll 1987; MacDermott and Weight 1982; Womack and Khodakhah 2002), including MNCs (Dopico et al. 1999), SK channel activation is responsible for the generation of the AHP following a train of action potentials (Armstrong et al. 1994; Bourque and Brown 1987; Greffrath et al. 1998; Kirkpatrick and Bourque 1996; Lancaster and Adams 1986; Lancaster and Nicoll 1987; Sah and Bekkers 1996). This apamin-sensitive AHP is intermediate between the fast AHP (~50 ms) and “slow” AHP (lasting >5 s) (Ghamari-Langroudi and Bourque 2004).

Activation of SK current was described by the Hill function:

$$m_{SK\infty}=[\mathrm{Ca}^{2+}]_{in}^{\varphi} / \left(K_{m,SK}^{\varphi}+[\mathrm{Ca}^{2+}]_{in}^{\varphi}\right),$$

where $[Ca^{2+}]_{in}$ is the intracellular Ca^{2+} concentration, $K_{m,SK}$ is *the* dissociation constant and ϕ is the Hill coefficient. The activation parameters of SK channels (Fig. 2(b)) were taken from data obtained in giant inside-out patches of *Xenopus* oocytes (Xia et al. 1998) showing that all SK-channel subtypes exhibit similar Ca^{2+} dose-response relationships, with a half-maximal activation of about 0.3 μM Ca^{2+} and a Hill coefficient of about 4 (0.32±0.03 μM and 5.0±0.6 for SK3 channels) (see Appendix).

BK channels are activated by an increase in intracellular $[Ca^{2+}]$ and by depolarization (Vergara et al. 1998), and the activation was described by a modified Boltzmann function:

$$m_{\mathrm{BK}\infty}(V,[\mathrm{Ca}^{2+}]_{\mathrm{in}}) = 1.0/[1.0+\exp[-(V - V_{\mathrm{half,BK}}([\mathrm{Ca}^{2+}]_{\mathrm{in}}))/\theta_{\mathrm{BK}}]],$$

where the half-activation voltage for the gating variable $V_{half,BK}([Ca^{2+}]_{BK})$ is a logarithmic function of intracellular Ca^{2+} concentration in the vicinity of the channel (see Appendix). Parameters of these channels in the model were based on data obtained in rat supraoptic MNCs (Dopico et al. 1999) (Fig. 2(c)).

Ca^{2+}-activated non-selective cation current: The model includes a Ca^{2+}-activated nonselective cation (CAN) current, which is present in neuronal cells (Partridge et al. 1994), including MNCs (Ghamari-Langroudi and Bourque 2002). Because CAN channels are usually nearly equally permeable to Na^+ and K^+ (see Teulon 2000), the CAN current was described in the model as the sum of Na^+ current and K^+ current with unitary conductance by the following equations:

$$I_{\mathrm{CAN}}=I_{\mathrm{Na,CAN}}+I_{K,\mathrm{CAN}};$$
$$I_{\mathrm{Na,CAN}}=G_{\mathrm{Na,CAN}}(V - E_{\mathrm{Na}});$$
$$I_{K,\mathrm{CAN}}=G_{\mathrm{Na,CAN}}(V - E_{\mathrm{K}}).$$

The unitary conductance

$$G_{\mathrm{CAN}}=G_{\mathrm{Na,CAN}}=G_{\mathrm{K,CAN}}=g_{\mathrm{CAN}} \cdot m_{\mathrm{CAN}}$$

was used in the description of the CAN current:

$$I_{\mathrm{CAN}}=g_{\mathrm{CAN}} \cdot m_{\mathrm{CAN}}(2V - E_{\mathrm{Na}} - E_{\mathrm{K}}),$$

where g_{CAN} is the maximal conductance for I_{CAN} and m_{CAN} is the activation function for I_{CAN} The Ca^{2+} and voltage-dependence of m_{CAN} in the model is described as the product of two functions:

$$m_{\mathrm{CAN}} = A([\mathrm{Ca}^{2+}]_{\mathrm{in}}) \cdot B(V, [\mathrm{Ca}^{2+}]_{\mathrm{in}}).$$

One of them is based on the Hill equation:

$$A([\mathrm{Ca}^{2+}]_{\mathrm{in}}) = ([\mathrm{Ca}^{2+}]_{\mathrm{in}})^2 / \left(([\mathrm{Ca}^{2+}]_{\mathrm{in}})^2 + \mathrm{K}^2_{d,\mathrm{CAN}}\right),$$

the other is based on the Boltzmann equation:

$$B(V, [\mathrm{Ca}^{2+}]_{\mathrm{in}}) = 1/(1+\exp(-(V+V_{\mathrm{CAN},h} \cdot S([\mathrm{Ca}^{2+}]_{\mathrm{in}}))/3)).$$

The function $S([\mathrm{Ca}^{2+}]_{\mathrm{in}})$ reflects the Ca^{2+}-sensitive shift of half-activation:

$$S_i = 1.0/\left(1+\exp\left(\left([\mathrm{Ca}^{2+}]_{\mathrm{in},i} - a_1\right)/b_1\right)\right) + 1.2/\left(1+\exp\left(\left([\mathrm{Ca}^{2+}]_{\mathrm{in},i} - a_2\right)/b_2\right)\right) - 5.9;$$

where $a_1 = 0.138 \cdot 10^{-3}$ mM; $b_1 = 0.5 \cdot 10^{-5}$ mM; $a_2 = 0.135 \cdot 10^{-3}$ mM; $b_2 = 0.7 \cdot 10^{-5}$ mM. This function provides a shift of half-activation of approximately −10 mV in the physiological range of intracellular $[Ca^{2+}]$. The Ca^{2+} dependence of half-activation is in correspondence with the findings of Bourque (1986), which showed that application of the Ca^{2+} channel antagonist Cd^{2+} strongly reduced the amplitude of the I_{DAP} and shifted the threshold of activation of this current toward a more positive membrane potential by approximately 10–15 mV. A Hill coefficient of 1 did not match the reported difference in the amplitudes of I_{DAP}(I_{CAN}) evoked by 5–8 spikes in control and with application of Cd^{2+} (see Bourque 1986). Therefore, a Hill coefficient of 2 and a dissociation constant ($K_{d,\mathrm{CAN}}$) of 300 nM were used in our model CAN current. The activation characteristics of the CAN current are described in Fig. 2(d,e).

SOR current: A slowly activated K^+ current underlying the sustained outward rectification (SOR) and rebound depolarization in OT neurons was included in each compartment of the model in order to simulate electrical properties of OT cells (Stern and Armstrong 1995, 1997; Teruyama and Armstrong 2002). Steady-state characteristics of activation of this current are presented in Fig. 2(a) (see also Appendix 1.3.3).

Ca^{2+} currents: In acutely dissociated magnocellular neurons from the rat SON, high-voltage activated L-, N-, P/Q- and R-type Ca^{2+} currents, but not the low-voltage activated T-type current, were observed (Joux et al. 2001). The T-type current has been observed in other studies of MNCs (Erickson et al. 1993; Fisher and Bourque 1995), but it appears not to play a prominent role in MNC electrophysiological properties (Luther and Tasker 2000) and, therefore, it was not included in the model. The L- and R-type currents are fast activating and slowly inactivating, whereas N- and P/Q-type currents are activated more slowly and are non-inactivating. For simplicity, we included only two voltage-gated Ca^{2+} currents, one of each type: the lower threshold and rapidly activating L-type current and the higher threshold and slower N-type current. Following the current/voltage relationships obtained by Joux et al.

(2001), activation of the N-type current was described by a single Boltzmann function, whereas activation of the L-type current was described by two Boltzmann functions (see Appendix). According to Joux et al. (2001), L-type calcium channels in MNCs can be formed by either Cav1.2 or Cav1.3. Each channel has its own voltage dependence. Immunocytochemical studies (Joux et al. 2001) showed that both of these subunits are present and have differential space distributions in MNCs. Experimental current-voltage relationships in MNCs were composed of at least two components, being best described by double Boltzmann functions with half-activation potentials around −30 and −10 mV (Joux et al. 2001). In our model we used double Boltzmann functions with half-activation potentials of −27 and −11.4 mV and slope factors of 4.5 and 2.0. These functions provided a good fit to the L-current experimental current/voltage relationship (Fig. 3(a2)). Each compartment has its own activation curve for the L-type current, and features a shoulder caused by summation of Boltzmann functions with different half activation potentials and slope factors (Fig. 2(f)). Parameters for inactivation of the L-type current and the distributions of L- and N-type conductances between compartments were selected to provide a fit to voltage clamp data obtained for the different Ca^{2+} current types and to reproduce the total Ca^{2+} current in the cell (Fig. 3). Compartmental specificity of the Ca^{2+} currents in the model is based on immunohistochemical evidence of the differential somato-dendritic distribution of $Ca_V1.2$ and $Ca_V1.3$ subunits (L-type channels) and $Ca_V2.2$ subunits (N-type channels) in magnocellular neurons described by Joux et al. (2001). In order to take into account the loss of distal dendrites in the dissociated cell preparation (Joux et al. 2001), the current/voltage relationships of the Ca^{2+} currents in the model were fitted to the experimental data obtained in dissociated cells assuming a loss of 80% of secondary dendrite length. In the model, the weights of the Boltzman functions for the L-type current activation equations in each compartment as well as parameters for inactivation equations were chosen such as to achieve the best agreement with voltage clamp experiments (Joux et al. 2001) (see Appendix).

2.1.3 Intracellular Ca^{2+} dynamics—The dynamics of intracellular $[Ca^{2+}]$ in each compartment ("*i*") is described by the first order equation:

$$d[\mathrm{Ca}^{2+}]_i/\mathrm{d}t = 2f_{\mathrm{Ca},i}\left(-(\sum I_{\mathrm{Ca},j,i})/(\mathrm{d}_i F) - U_i\left([\mathrm{Ca}^{2+}]_i - [\mathrm{Ca}^{2+}]_r\right)\right),$$

where $f_{Ca,i}$ is the endogenous Ca^{2+} buffer capacity, a measure of how fast $[Ca^{2+}]$ changes in the compartment; $\Sigma I_{Ca,j}$ is the total Ca^{2+} current (subscript "j" represents the L- or N-type Ca^{2+} current in the compartment); U_i is the rate constant of Ca^{2+} uptake by intracellular stores; $[Ca^{2+}]_r$ is the intracellular $[Ca^{2+}]$ at rest; d_i is the diameter of the compartment; and F is the Faraday constant.

The specificity of coupling between Ca^{2+} channels and Ca^{2+}-activated K^+ channels has been demonstrated in hippocampal neurons (Marion and Tavalin 1998), where N-type Ca^{2+} channels preferentially activate BK channels, while L-type channels activate SK channels. The temporal association of the opening times of N-type channels and BK channels indicates that these channels are in close proximity to one another. Taking into account the results of studies showing that, in hippocampal pyramidal neurons, BK channel distribution decreases with the distance from the soma (Johnston et al. 2000), we did not include BK channels in the secondary dendrites of our model. We assumed that the $[Ca^{2+}]$ in the vicinity of BK channels changed much faster than the bulk $[Ca^{2+}]$ in the compartment. Therefore, additional Ca^{2+} subcompartments (subdomains) for BK channels were added to the soma and primary dendrites (Fig. 1(b)) according to the following formalism:

$$d[\mathrm{Ca}^{2+}]_{\mathrm{BK},i}/\mathrm{d}t = 2f_{\mathrm{Ca,BK},i}(-I_{\mathrm{Ca},N,i}/(r\mathrm{d}_i F) - K_{\mathrm{BK},i}([\mathrm{Ca}^{2+}]B_{K,i} - [\mathrm{Ca}^{2+}]_r)),$$

where $[Ca^{2+}]_{BK,i}$ is the $[Ca^{2+}]$ that activates BK channels, $f_{Ca,BK}$ is the fast endogenous Ca^{2+} buffering capacity in the vicinity of BK channels, $K_{BK,i}$ is the rate constant of $[Ca^{2+}]$ decay in the subcompartment, and r is the ratio of BK subcompartment volume to the total compartment volume. Here, "i" can be either "s" (soma) or "pd" (primary dendrite). The simulated dynamics of $[Ca^{2+}]$ in the BK subcompartment triggers the activation of the BK current during spike development and plays a role in spike AHP.

2.2 Model implementation

Numerical integrations of simulations were performed using an implicit Runge-Kutta method of order five with a variable time step (Hairer and Wanner 1996). The symmetrical structure of the model allows one to perform numerical computations for three compartments only, the soma, the primary dendrite, and the secondary dendrite. The dynamics of membrane potential and $[Ca^{2+}]$ in the three compartments were described by a total of 39 first-order differential equations. The simulations were run on a 700 MHz R16000 SGI Origin 350 and a 360 MHz R12000 SGI Octane2 workstation.

3 Results

3.1 Action potential generation and calcium dynamics

To date there are no direct recordings from the dendrites of MNCs, so we based the selection of the distributions of conductances on experimental data obtained from other nerve cells. Somatic and dendritic recordings in hippocampal CA1 pyramidal neurons have shown that somatic spikes in these cells are larger than dendritic spikes (Callaway and Ross 1995). Also, a prominent gradient in the density of the A-type current exists in CA1 pyramidal neurons (Hoffman et al. 1997; Golding and Spruston 1998). While in our model the conductance for $I_{K(DR)}$ is distributed uniformly, the conductance for the sodium current is larger in the soma and the proximal dendrites than in the distal dendrites ($g_{Na,s}$: $g_{Na,pd}$:$g_{Na,sd}$ =7:5:1); the conductance for the transient potassium current has the opposite distribution ($g_{A,s}$:$g_{A,pd}$: $g_{A,sd}$≈1:5:7). The selected set of conductances provided a spike amplitude and duration similar to those recorded with somatic recordings from MNCs. Magnocellular neurons have action potentials with a fast ascending phase that provides a peak amplitude of 77.8±2.0 mV in VP neurons and 73.2±1.8 mV in OT neurons and a duration at the half-maximum spike amplitude of 1.5±0.1 ms (Armstrong et al. 1994). Figure 4 shows the voltage-gated currents and action potentials generated in the different compartments of the model MNC. In the model, spikes have a peak amplitude of 75 mV and a duration at the half-maximum spike amplitude of 1.2 ms, which are values close to the average values measured experimentally (Armstrong et al. 1994; Bourque and Renaud 1985; Stern and Armstrong 1996; Tasker and Dudek 1991; Teruyama and Armstrong 2002). In the model, action potentials and ionic currents have different characteristics in the soma, primary dendrite and secondary dendrite. Under simulated somatic stimulation with a depolarizing current of +25 pA, the initiation of the somatic spike and the spike in the primary dendrite precedes significantly (by about 0.4 ms) spike initiation in the secondary dendritic compartment (Fig. 4(a)). Also, the amplitude of the spike in the distal dendrites is decreased to 49 mV. The model neuron demonstrates notable differences in the compartmental dynamics of voltage-gated ionic currents with action potential generation in the soma and in the primary and secondary dendrites (Fig. 4(b)) due to the differences in the parameters of each of these compartments (see Section 2.1 and Appendix). Thus, the A-current

makes a bigger contribution to membrane repolarization during the descending phase of the action potential in the dendrites than in the soma.

It has been established in calcium imaging studies that the dendrites of different types of nerve cells exhibit larger-amplitude Ca^{2+} spikes and more rapid Ca^{2+} accumulation and decay than the soma (Wilson and Callaway 2000; Abel et al. 2004). Some differences in Ca^{2+} dynamics have also been revealed in different compartments of MNCs during and after evoked bursts with spike frequencies of 5–10 Hz (Roper et al. 2004). Thus, dendritic Ca^{2+} concentration rises faster and stays higher in the dendrites compared to the soma of MNCs during 2–3 s of the spike discharge, and the dendritic Ca^{2+} concentration decays more rapidly than the somatic Ca^{2+} concentration following the spike discharge. In the model, the different volume-to-surface ratios of the soma, primary dendrites and secondary dendrites, as well as the differential spatial distributions of voltage-gated Ca^{2+} channels and Ca^{2+} uptake by stores (Table 1) provide specificity of Ca^{2+} dynamics in the different compartments that are consistent with experimental data. During spike trains, each action potential makes a contribution to the rising Ca^{2+} concentration, as shown in Fig. 5(a,b).

3.2 Simulation of the basic electrophysiological properties of MNCs

3.2.1 Transient outward rectification—When hyperpolarized, MNCs respond to depolarizing current injections with an I_A-mediated transient outward rectification (TOR) (Bourque 1988; Fisher et al. 1998; Luther and Tasker 2000), which is characterized by a slowing of membrane charging and a delay to the onset of the first action potential (Fig. 6(a)). Under the same simulated protocol, the model MNC shows a similar dampening of the depolarization and delayed onset of spike firing (Fig. 6(b)). The model shows a “notch” in the rising phase of the voltage transient characteristic of the strong TOR generated in MNCs (Tasker and Dudek 1991; Luther and Tasker 2000; Luther et al. 2000). Figure 6(c) depicts the dynamics of the model variables underlying the behavior of I_{Na}(m^3 and h) and I_A(p^4 and q) during the time course of V_s from the onset of the depolarizing current to the end of the first spike, as shown in Fig. 6(b) (red trace). The corresponding time span of 150 ms is marked by the blue bar in Fig. 6(b). The relatively fast activation (p variable) of I_A and its slow inactivation (q variable) prevent development of the first spike.

3.2.2 Depolarizing after potential—Magnocellular neurons exhibit depolarizing after potentials (DAPs) after single spikes or brief trains of spikes (Andrew and Dudek 1984a; Bourque and Renaud 1985). The summation of DAPs causes a small plateau potential and an after-discharge of spikes, which are dependent on the stimulation protocol, the physiological state of the neuron (i.e., from virgin, pregnant, or lactating rats), and the type of magnocellular neuron (i.e., OT or VP neuron) (Stern and Armstrong 1996; Teruyama and Armstrong 2002). The calcium and voltage dependence of the I_{DAP} in MNCs has been established (Bourque 1986), however its ionic mechanisms remain uncertain. There are two possible ionic mechanisms for the DAP in MNCs proposed on the basis of experimental findings. One involves the Ca^{2+}-dependent block of a resting K^+ conductance, presumably TASK-1, producing a brief depolarizing shift in the cells’ resting potential (Li and Hatton 1997a,b; Roper et al. 2003). Our model is based on a second possible mechanism, activation of a calcium-dependent, non-specific cation (CAN) current, based on the sensitivity of DAPs and phasic firing in SON neurons to flufenamic acid, a blocker of CAN channels (Ghamari-Langroudi and Bourque 2002) (see Section 4). The main characteristics of CAN channels are their conductance between 18 and 34 pS, their lack of discrimination between monovalent cations, their low permeability to Ca^{2+}, their sensitivity to intracellular [Ca^{2+}], their inhibition by cytosolic ATP, and their blockade by flufenamic acid (for review see Teulon 2000).

The DAP is expressed in the majority (75%) of VP neurons, whereas it is present in only a minority (32%) of OT neurons recorded in the brain slice preparation (Armstrong et al. 1994). The findings of Greffrath et al. (1998) suggest that the induction, maintenance and termination of the plateau potential underlying bursting in MNCs are regulated by the balance between the DAP and the slow AHP. Experimental evidence of a contribution of the slow AHP to burst termination was presented by Ghamari-Langroudi and Bourque (2004). However, the best characterized mechanism for burst termination is an activity-dependent inhibition of the DAP (Brown and Bourque 2004; Brown et al. 2006), which was incorporated in the model of Roper et al. (2004). In slice experiments, about half of the MNCs encountered in the SON displayed a DAP (Armstrong et al. 1994; Li et al. 1995). Only a small proportion (16%) of dissociated MNCs isolated from the rat SON displayed DAPs or spontaneous bursting activity following brief current-evoked trains (Oliet and Bourque 1992). These cells usually retained one to three short (<30 μm) processes. These findings suggest that the dendrites play an important role in DAP generation. Since CAN channel activation depends on intracellular $[Ca^{2+}]$, the distribution of g_{CAN} between model compartments may have a significant influence on the DAP. The values of $g_{CAN,s}$=45 μS/cm^2, $g_{CAN,pd}$=90 μS/cm^2 and $g_{CAN,sd}$=0 provided the best correspondence between simulated and experimental data (Bourque 1986; Li and Hatton 1997b) (Fig. 7(a–d)). Simulated blockade of this current by setting $g_{CAN,i}$ to zero (Fig. 7(e)) reproduced the results of experiments with application of flufenamic acid to MNCs (Ghamari-Langroudi and Bourque 2002).

3.2.3 After hyperpolarizing potential and spike frequency adaptation—OT and VP neurons exhibit a prominent AHP following trains of action potentials evoked with long-lasting stimulation (Andrew and Dudek 1984b; Armstrong et al. 1994; Bourque et al. 1985). The size of the AHP is dependent upon the number of spikes in the train. The application of the SK channel blocker, apamin, strongly inhibits the AHP (Armstrong et al. 1994). Figure 8 shows the AHP and Ca^{2+} dynamics in the model that match data obtained in experiments with prolonged stimulation of MNCs in slice preparations and simultaneous recordings of membrane potential and $[Ca^{2+}]$ in the soma (Roper et al. 2003). The model neuron is able to simulate AHPs evoked by long-lasting stimulation (Armstrong et al. 1994; Stern and Armstrong 1996; Teruyama and Armstrong 2002) as well as spike frequency adaptation similar to that observed experimentally in MNCs (Stern and Armstrong 1996; Tasker and Dudek 1991; Teruyama and Armstrong 2002). This phenomenon is caused by the SK current underlying the AHP (Fig. 8(c)); the simulated blockade of SK channels eliminated spike frequency adaptation.

3.2.4 Sustained outward rectification and rebound depolarization—Magnocellular OT-secreting neurosecretory cells, but not VP-secreting cells, demonstrate a depolarization-activated sustained outward rectification (SOR) (Stern and Armstrong 1995, 1997; Teruyama and Armstrong 2002). The SOR is observed as a sag in the voltage trajectory during hyperpolarizing pulses from a depolarized holding potential, and as a rebound depolarization that supports action potentials following the hyperpolarizing pulses. The SOR is present positive to −75 mVand decreases in amplitude as the hyperpolarizing pulses approach the potassium equilibrium potential (E_K). The SOR has been proposed to be the result of the deactivation of a voltage-dependent, non-inactivating K^+ current (Stern and Armstrong 1995).

In our model, I_{SOR} is described as a slowly activating K^+ current using Hodgkin-Huxley formalism (see Appendix). The steady-state activation of I_{SOR} is described as a Boltzmann function, with the time constant of activation ($\tau_{m,SOR}$) equal to 350 ms. Specific conductances for I_{SOR} in all compartments were equal ($g_{SOR,s} = g_{SOR,pd} = g_{SOR,sd}$ = 20 μS/cm^2), simulating a uniform distribution of channels. This representation of the SOR current is similar to the one in the single compartment model of Roper et al. (2003), but our set of parameters was selected

to provide the best fit to experimental I–V curves (Stern and Armstrong 1995) in our multicompartmental model (Fig. 9). The redistribution of channels between compartments had no significant influence on the SOR characteristics (data not shown).

3.3 Role of the SOR Current in the AHP

Although it was not the purpose of this study to systematically simulate all the differences in the electrophysiological properties of VP and OT neurons, our model suggests that the expression of SOR in MNCs may be a critical factor underlying the differences in the dynamics of AHPs between OT and VP neurons. Figure 10(a) shows experimental records of AHPs in a VP neuron (*A1*) and an OT neuron (*A2*) evoked by short depolarizing current pulses (Armstrong et al. 1994). Membrane potential changes in response to the same stimulation protocol in two models of MNCs are presented in Fig. 10(b). All the parameters for the two models were the same, except for the DAP and SOR parameters. The model VP neuron included the I_{DAP} (generated by a CAN current), but no I_{SOR}. The model OT neuron included the I_{SOR}, but no I_{DAP}. The respective OT and VP neuron models simulated distinct AHPs, with differences in time constants of decay and dynamics similar to those observed experimentally (Armstrong et al. 1994; Teruyama and Armstrong 2002). Thus, in the model OT neuron, the τ_{AHP} is 188 ms, while in experiments on OT neurons in hypothalamic explants, the τ_{AHP} was found to be 257±73 ms; in the model VP neuron the τ_{AHP} is 424 ms, while in experiments on VP neurons, the τ_{AHP} value was 431±93 ms (Armstrong et al. 1994) (Fig. 10(b)).

3.4 Effects of compartmental distribution of ion conductances on the electrophysiological properties of the model neuron

Because of the lack of experimental data on the somato-dendritic distribution of ion channels in MNCs and its impact on MNC electrical activity, we studied the effects of the redistribution of some intrinsic ion conductances among the three compartments on the model's response to typical experimental stimulation protocols. Other than the conductances that were redistributed in the specific simulations (g_A, g_{CAN} and g_{SK}), all other parameters of the model were held constant at the values indicated in Table 1.

3.4.1 Distribution of g_A—In the model, the simulated A-type channel density increases with the distance from the soma ($g_{A,s}$:$g_{A,pd}$:$g_{A,sd}$≈1:5:7), similar to what has been observed in hippocampal CA1 pyramidal neurons (Hoffman et al. 1997) and in mitral/tufted cells (Bischofberger and Jonas 1997). We found that the compartmental distribution of A-current channels has a marked influence on the frequency of evoked spiking in the model neuron. We tested the effect on spiking of changing the compartmental distribution of the A-current conductance while keeping the total membrane conductance, $A_s g_{A,s}+2\,A_{pd} g_{A,pd}+4A_{sd} g_{A,sd}$, constant (where A_s, A_{pd}, and A_{sd} are the surface areas of the soma, primary dendrites, and secondary dendrites, respectively) (Fig. 11(b)). A similar approach was used for the redistribution of other conductances (g_{CAN} and g_{SK}). Figure 11(a) shows typical high frequency spiking in a VP neuron recorded experimentally in vitro in response to depolarization. Distributions of A-current conductances that were predominantly dendritic (Fig. 11(b1,b6,b7)) produced repetitive spiking activity that is similar to that observed experimentally (Fig. 11(c1, c6,c7)). Somatic, primary dendritic or uniform distributions of g_A (Fig. 11(b2–c2,b3–c3,b4–c4,b5–c5)) caused a delay in the onset of each successive action potential and a decrease in the frequency of action potentials, resulting in an evoked spiking activity that differed from that of MNCs recorded experimentally in vitro under the same stimulation protocol (Fig. 11(a)).

3.4.2 Distribution of the DAP conductance (g_{CAN})—We simulated the expression of CAN channels in the model MNC, which allowed us to reproduce DAPs and spike after-discharges following short depolarizing pulses similar to those observed experimentally (Fig.

12) (Li and Hatton 1997a). With all other conductances and the total CAN conductance maintained constant, the simulated compartmental distribution of CAN channels in the soma and primary dendrites gave the best correspondence with the DAP amplitude and dynamics observed in MNCs recorded in slices ($g_{CAN,s}$=45 μS/cm^2, $g_{CAN,pd}$=90 μS/cm^2 and $g_{CAN,sd}$=0 (Fig. 12(b1,c1))).

3.4.3 Distribution of the AHP conductance (g_{SK})—The possible role of SK channel distribution in AHP generation was also studied in the model MNC. A good correspondence with the AHP recorded in VP neurons in vitro (Armstrong et al. 1994; Teruyama and Armstrong 2002) was obtained in the model (without I_{SOR}) with a compartmental distribution of the SK conductance of $g_{SK,s}$= 10 μS/cm^2, $g_{SK,pd}$=40 μS/cm^2 and $g_{SK,sd}$=25 μS/cm^2, (Fig. 13(c1,d1)) as well as with uniform distribution of the g_{SK} throughout all three compartments (Fig. 13 (c2,d2)), with SK channels distributed only in primary and secondary dendrites (Fig. 13 (c6,d6)), and with SK channels expressed only in secondary dendrites (Fig. 13(c7,d7)). On the other hand, SK channels located in the soma only (Fig. 13(c3, d3)), in the soma and primary dendrites (Fig. 13(c4,d4)) and in the primary dendrites only (Fig. 13(c5,d5)) produced a much slower decay of the AHP than has been observed in MNCs experimentally (Fig. 13(a,b)). The model's SK channel distribution (Fig. 13(c1)) was selected based on these data and data generated with other stimulation protocols (Figs. 8(a) and 10(b)) that provided the best match to experimental data.

4 Discussion

4.1 Compartmentalization of properties in the model

During the last decade it has become evident that dendrites of nerve cells are dynamic structures that express voltage-gated ion channels and actively participate in the generation of neuronal electrical activity (for review see Häusser et al. 2000). Electrophysiological evidence of active dendritic properties has been obtained in brain structures like the hippocampus and neocortex, where neuronal architecture makes dendrites of nerve cells accessible experimentally. Such direct experimental measurements in the hypothalamus are more difficult because the dendrites of MNCs are interwoven with somata and axons. However, indirect studies have suggested a differential expression of ion currents in the soma and dendrites of MNCs (Bains 2002; Mason and Leng 1984). Therefore, a multicompartmental model of MNCs would be useful for studying the electrophysiological mechanisms that rely on differential somato-dendritic properties in these cells.

We designed a seven-compartment model of the hypothalamic MNC using basic morphological parameters of these neurons, experimentally measured passive electrical properties, and a compartmentalized distribution of ionic currents and Ca^{2+} dynamics based on experimental observations. The activation and inactivation properties of voltage-gated currents were extracted from available voltage-clamp data from MNCs (Joux et al. 2001; Luther and Tasker 2000; Tanaka et al. 1999), and from other types of mammalian CNS neurons (Hoffman et al. 1997; Migliore and Shepherd 2002). The main criteria for determining the distribution of channels were simulations of appropriate physiological responses for MNCs for different experimental protocols. The model closely reproduces the basic electrophysiological properties of MNCs *in vitro*. This multi-compartmental model expands on a recently proposed single-compartment model (Roper et al. 2003) to allow us to investigate the putative roles of compartmentally distributed ion currents and intracellular Ca^{2+} dynamics in shaping the electrophysiological properties of MNCs.

The simulated Ca^{2+} dynamics in the different parts of our model neuron are close to those observed experimentally in recorded MNCs in amplitude and time constant of decay (Roper et al. 2003, 2004) and are similar to analogous results of Ca^{2+} imaging studies done in other

types of neurons (Abel et al. 2004; Wilson and Callaway 2000). In addition to L- and N-type Ca^{2+} currents, our model includes two Ca^{2+} subcompartments for activation of BK channels in the soma and primary dendrites that are separated by barriers from the cytoplasm. The physiological basis of these calcium microdomains is the experimentally observed colocalization of Ca^{2+} channels and BK channels, which suggests that BK channels are activated by a fast increase in $[Ca^{2+}]$ delivered in close proximity to the channels (Marion and Tavalin 1998; Sun et al. 2003). Thus, changes in $[Ca^{2+}]$ in these structurally and functionally small subcompartments are larger than in the bulk cytoplasm.

4.2 Compartmentalization of the A-current

In the model, I_A is most prominent in the secondary dendrites due to the increase in the maximum conductance of this current with distance from the soma ($g_{A,s}<g_{A,pd}<g_{A,sd}$), similar to that observed in hippocampal pyramidal neurons (Hoffman et al. 1997; Johnston et al. 2000). The Atype current may increase in the dendrites due not only to a corresponding increase in the density of Kv4-family α-subunits that form A-type channels, but also to changes in the distribution of Kv-channel interacting proteins (KChIPs), which may augment I_A by a variety of mechanisms (An et al. 2000). For simplicity we did not account for changes in channel properties in different model compartments and showed only how the subcellular distribution of uniform A-type channels influences the spiking characteristics of MNCs (Fig. 11).

The presence of A-type channels in the dendrites of MNCs in PVN and SON has been suggested by the finding that these neurons appear to lose their I_A after dissociation and the resulting loss of their dendritic trees (Widmer et al. 1997). Also, experiments with immunocytochemical identification of dissociated MNCs revealed that the A-type current was selectively expressed in OT-neurophysin-positive cells (Widmer et al. 1997). Taking into account that experiments in hypothalamic slices show that A-type channels are expressed in both VP and OT neurons (see Armstrong and Stern 1998), these results, taken together, suggested that A-type channels may be expressed only in the dendritic tree of VP neurons. However, in a series of experiments by Fisher et al. (1998), an A-type current was recorded in both VP and OT neurons following acute isolation and loss of their dendritic trees, implying a soma/primary dendrite localization of the A-type channels in both types of MNCs. In our modeling study, available experimental data on A-current characteristics were taken into account (Luther and Tasker 2000). We found that the best correspondence between model and spiking activity recorded in MNCs was achieved with a primarily dendritic distribution of A-type channels (Fig. 11). While somatic, somato-primary dendritic, primary dendritic only and uniform distributions of A-type channels did not produce spiking patterns similar to that seen in MNCs, both dendritic-only and increasing somatic-to-dendritic distributions produced spike patterns that resembled MNC spiking activity.

4.3 Ionic and compartmental mechanisms of the DAP

There are considerable discrepancies in the experimental data concerning the ionic mechanisms responsible for the DAP in MNCs. Two mechanisms have been proposed and backed up with experimental findings: the blockade of a resting K^+ current (Li and Hatton 1997a) and the generation of a Ca^{2+}-dependent, non-selective cation, or CAN, current (Ghamari-Langroudi and Bourque 2002). We selected the CAN current mechanism in our model for the following reasons. First, there is no experimental evidence for the inhibition of resting K^+ channels, presumably TASK-1 channels, by intracellular Ca^{2+}, and experimental manipulation of the intracellular $[Ca^{2+}]$ in both directions fails to influence the activity of TASK channels (Duprat et al. 1997; Lenoudakis et al. 1998). These channels have relative voltage independence and rapid activation with little or no inactivation following depolarization, as judged by their opening across the physiological range of membrane potentials (Lesage and Lazdunski 2000; Goldstein et al. 2001). Therefore, these properties of TASK-1 channels make it unlikely that

resting K^+ channels are responsible for the DAP. On the other hand, there are several lines of evidence that support the role of a CAN current in mediating the DAP. CAN channels exist in the membranes of a variety of mammalian cells, both excitable and non-excitable, and support important cellular responses such as neuronal bursting, secretion, and cardiac rhythmicity (Siemen 1993; Thorn and Petersen 1993; Partridge et al. 1994; Teulon 2000). For example, CAN channels take part in plateau potential generation and persistent spiking in entorhinal cortex neurons (Egorov et al. 2002), in DAPs in myenteric neurons (Vogalis et al. 2002), and in after-depolarization and burst after discharge in rat neocortical neurons (Kang et al. 1998; Aoyagi et al. 2002). I_{CAN} appears to have higher calcium sensitivity than other Ca^{2+}-activated currents, such as I_{BK} and I_{SK} (Zhu et al. 2004). The voltage-dependence of opening of CAN channels recently was reported in several excitable cells, including in rat and human cardiomyocytes (Guinamard et al. 2002, 2004) and in hamster vomeronasal sensory neurons (Liman 2003). We included these voltage-dependent properties in our mathematical description of I_{CAN} (see Appendix). Thus, based on the combined Ca^{2+} dependence and voltage sensitivity of these channels, we regarded the CAN channel hypothesis (Ghamari-Langroudi and Bourque 2002) to be the most plausible one for the DAP mechanism. Further support of this hypothesis came from the recent finding that ~30% of cell-attached patches on isolated SON MNCs contained nonselective cation channels that were active at rest (Han et al. 2003). Also, recent experimental studies with whole cell recordings in both current and voltage clamp demonstrated that VP cells in the SON express a CAN current, whose activation contributes to the generation of the DAP (Teruyama and Armstrong 2006).

No data are available concerning the distribution of CAN channels in different parts of neurons, however our modeling study allows one to draw the conclusion that this distribution may play an important role in the generation of DAPs in MNCs. In our model, the activity-dependent rise and decay in intracellular $[Ca^{2+}]$ are fastest in the secondary dendrites and slowest in the soma, which is in agreement with spatial $[Ca^{2+}]$ measurements and recordings from MNCs (Roper et al. 2004). The best correspondence to recorded DAPs (Fig. 12(a)) was observed when CAN channels were located in the primary dendrites and soma, with more prominent expression in the primary dendrites (Fig. 12(b1,c1)). Simulated redistribution of CAN channels from the soma to the dendrites leads to an increase in the amplitude of the DAP, but also to an increase in its decay rate (Fig. 12(b4–b6,c4–c6)), which is not consistent with experimental data. A similar result was obtained with a uniform distribution of CAN channels in all three compartments of the cell (Fig. 12(b7,c7)). Redistribution of CAN channels to the soma slightly decreases the amplitude of the DAP and significantly increases its decay time (Fig. 12(b3, c3)), which also is not consistent with the experimental data. These results suggest that the expression of CAN channels in different parts of the cell may be important for burst initiation and persistent spiking activity in MNCs. Since the best match to experimental data was achieved when the CAN channels underlying the DAP were restricted to the primary dendrites and soma, our findings suggest that the majority of acutely dissociated MNCs did not display DAPs and DAP-mediated bursting (Oliet and Bourque 1992) because of the loss of dendrites caused by cell dissociation.

4.4 Ionic and compartmental mechanisms of the AHP

In our model, the AHP is mediated by a SK current, which is activated by elevation of intracellular $[Ca^{2+}]$. Differences in the compartmental $[Ca^{2+}]$ dynamics provide the potential for differences in AHP generation and decay by changing the I_{SK} conductance among the compartments. The model allows one to fit the AHP to experimental data from magnocellular neurons (Armstrong et al. 1994; Stern and Armstrong 1996; Teruyama and Armstrong 2002) and suggests mechanisms of regulation of the AHP not only by varying channel properties, but also by changing compartmental $[Ca^{2+}]$ dynamics and SK channel distribution.

The finding that dissociated MNCs (i.e., without dendrites or with short primary dendrites) express a Ca^{2+}-dependent K^+ conductance (Oliet and Bourque 1992) similar to that found in neurons recorded in slices (Armstrong 1995; Andrew and Dudek 1984b; Bourque and Renaud 1985) suggests that the channels responsible for the AHP are located primarily in the soma and primary dendrites. Our results of changing the compartmental distribution of the SK channels in the model suggest that these channels are probably not located exclusively in the soma or in the soma and primary dendrites, but rather are distributed among the somatic, primary dendritic and secondary dendritic compartments (Fig. 13(a)), since these distributions provide waveforms and decay time constants of the AHP that most closely approximate those of recorded MNCs under different stimulation protocols. Also, our findings show that the different AHP dynamics reported for OT and VP neurons (Armstrong et al. 1994; Teruyama and Armstrong 2002) may be due not only to the differential expression and distribution of SK channels, but also to the selective expression of the SOR current in OT neurons (see Fig. 10).

4.5 Model limitations

Construction of a mathematical model is always limited by available experimental data and adequate complexity. The characteristics of some currents were not available from MNC experimental data. This gap was filled by the adoption of data obtained from other mammalian CNS neurons, as well as by fitting characteristics of currents to obtain realistic model responses. In our model, simple first order differential equations were used for the description of Ca^{2+} dynamics in each compartment and sub-compartment. Intra- and intercompartmental diffusion was not taken into account. We did not completely explore the parameter space of the model; the analyses were done based on changes of one parameter and, therefore, other possible physiologically plausible solutions may exist. Possible ways to tune parameters of the model include the systematic sampling of the parameter space (Prinz et al. 2003) or evolution strategy with a fitness function based on phase-plane analysis (Achard and De Schutter 2006).

4.6 Conclusions

Our model provides a multicompartmental computational tool that takes into account MNC morphology and electrotonic properties, and includes a set of realistic voltage-gated and Ca^{2+}-activated ionic currents with authentic activation and inactivation characteristics. The model reproduces several of the hallmarks of MNC electrophysiological properties, including TOR, spike-frequency adaptation, AHPs, SOR, DAPs and DAP-mediated after discharges. The multiple compartments and different compartmental distributions of ionic conductances in our model provide a more realistic computational environment than single compartment models of MNCs. In particular, it is possible in our model to take into account differences in electrical properties between the soma and dendrites. Thus, the model allowed us to probe how the expression and spatial distribution of different ion channels influences the spiking properties of these neurons. The model, therefore, provides a framework for making realistic predictions concerning specific electrophysiological properties of MNCs.

Acknowledgments

We thank Dr. Cherif Boudaba for providing recordings of MNC spiking activity. This work was supported by U.S. Department of Energy Grant DE-FG02-01ER63119 (to the Tulane University Center for Computational Science), and National Institutes of Health grants NS039099 (to J. G. Tasker) and HL063195 (to N.A. Trayanova).

References

Abel HJ, Lee JC, Callaway JC, Foehring RC. Relationships between intracellular calcium and after hyperpolarizations in neocortical pyramidal neurons. Journal of Neurophysiology 2004;91:324–335. [PubMed: 12917389]

Achard P, De Schutter E. Complex parameter landscape for a complex neuron model. PLoS Comput Biol 2006;2:e94. [PubMed: 16848639]

An WF, Bowlby MR, Betty M, Cao J, Ling HP, Mendoza G, et al. Modulation of A-type potassium channels by a family of calcium sensors. Nature 2000;403:553–556. [PubMed: 10676964]

Andrew RD, Dudek FE. Analysis of intracellularly recorded phasic bursting by mammalian neuroendocrine cells. Journal of Neurophysiology 1984a;51:552–566. [PubMed: 6321696]

Andrew RD, Dudek FE. Intrinsic inhibition in magnocellular neuroendocrine cells of rat hypothalamus. Journal of Physiology 1984b;353:171–185. [PubMed: 6090639]

Aoyagi T, Kang Y, Terada N, Kaneko T, Fukai T. The role of Ca^{2+}-dependent cationic current in generating gamma frequency rhythmic bursts: Modeling study. Neuroscience 2002;115:1127–1138. [PubMed: 12453485]

Armstrong WE. Morphological and electrophysiological classification of hypothalamic supraoptic neurons. Progress in Neurobiology 1995;47:291–339. [PubMed: 8966209]

Armstrong WE, Smith BN, Tian M. Electrophysiological characteristics of immunochemically identified rat oxytocin and vasopressin neurones in vitro. Journal of Physiology 1994;475:115–128. [PubMed: 8189384]

Armstrong WE, Stern JE. Electrophysiological and morphological characteristics of neurons in perinuclear zone of supraoptic nucleus. Journal of Neurophysiology 1997;78:2427–2437. [PubMed: 9356394]

Armstrong WE, Stern JE. Electrophysiological distinctions between oxytocin and vasopressin neurons in the supraoptic nucleus. Advances in Experimental Medicine and Biology 1998;449:67–77. [PubMed: 10026787]

Bains JS. Dendritic action potentials in magnocellular neurons. Progress in Brain Research 2002;139:225–234. [PubMed: 12436938]

Bischofberger J, Jonas P. Action potential propagation into the presynaptic dendrites of rat mitral cells. Journal of Physiology 1997;504:359–365. [PubMed: 9365910]

Boudaba C, Di S, Tasker JG. Presynaptic noradrenergic regulation of glutamate inputs to hypothalamic magnocellular neurones. Journal of Neuroendocrinology 2003;15:803–810. [PubMed: 12834442]

Bourque CW. Calcium-dependent spike after-current induces burst firing in magnocellular neurosecretory cells. Neuroscience Letters 1986;70:204–209. [PubMed: 3774226]

Bourque CW. Transient calcium-dependent potassium current in magnocellular neurosecretory cells of the rat supraoptic nucleus. Journal of Physiology 1988;397:331–347. [PubMed: 2457699]

Bourque CW, Brown DA. Apamin and d-tubocurarine block the after hyperpolarization of rat supraoptic neurosecretory neurons. Neuroscience Letters 1987;82:185–190. [PubMed: 3696492]

Bourque CW, Randle JC, Renaud LP. Calcium-dependent potassium conductance in rat supraoptic nucleus neurosecretory neurons. Journal of Neurophysiology 1985;54:1375–1382. [PubMed: 4087038]

Bourque CW, Renaud LP. Activity dependence of action potential duration in rat supraoptic neurosecretory neurons recorded in vitro. Journal of Physiology 1985;363:429–439. [PubMed: 3926995]

Brimble MJ, Dyball RE. Characterization of the responses of oxytocin- and vasopressin-secreting neurones in the supraoptic nucleus to osmotic stimulation. Journal of Physiology 1977;271:253–271. [PubMed: 562405]

Brown CH, Bourque CW. Autocrine feedback inhibition of plateau potentials terminates phasic bursts in magnocellular neurosecretory cells of the rat supraoptic nucleus. Journal of Physiology 2004;557:949–960. [PubMed: 15107473]

Brown CH, Leng G, Ludwig M, Bourque CW. Endogenous activation of supraoptic nucleus kappa-opioid receptors terminates spontaneous phasic bursts in rat magnocellular neurosecretory cells. Journal of Neurophysiology 2006;95:3235–3244. [PubMed: 16495366]

Callaway JC, Ross WN. Frequency-dependent propagation of sodium action potentials in dendrites of hippocampal CA1 pyramidal neurons. Journal of Neurophysiology 1995;74:1395–1403. [PubMed: 8989380]

Canavier CC. Sodium dynamics underlying burst firing and putative mechanisms for the regulation of the firing pattern in midbrain dopamine neurons: A computational approach. Journal of Computational Neuroscience 1999;6:49–69. [PubMed: 10193646]

Chevaleyre V, Moos FC, Desarmenien MG. Correlation between electrophysiological and morphological characteristics during maturation of rat supraoptic neurons. European Journal of Neuroscience 2001;13:1136–1146. [PubMed: 11285011]

Dopico AM, Widmer H, Wang G, Lemos JR, Treistman SN. Rat supraoptic magnocellular neurones show distinct large conductance, Ca^{2+}-activated K^+ channel subtypes in cell bodies versus nerve endings. Journal of Physiology 1999;519:101–114. [PubMed: 10432342]

Duprat F, Lesage F, Fink M, Reyes R, Heurteaux C, Lazdunski M. TASK, a human background K^+ channel to sense external pH variations near physiological pH. EMBO Journal 1997;16:5464–5471. [PubMed: 9312005]

Egorov AV, Hamam BN, Fransen E, Hasselmo ME, Alonso AA. Graded persistent activity in entorhinal cortex neurons. Nature 2002;420:173–178. [PubMed: 12432392]

Erickson KR, Ronnekleiv OK, Kelly MJ. Role of a T-type calcium current in supporting a depolarizing potential, damped oscillations, and phasic firing in vasopressinergic guinea pig supraoptic neurons. Neuroendocrinology 1993;57:789–800. [PubMed: 8413816]

Fisher TE, Bourque CW. Voltage-gated calcium currents in the magnocellular neurosecretory cells of the rat supraoptic nucleus. Journal of Physiology 1995;486:571–580. [PubMed: 7473220]

Fisher TE, Voisin DE, Bourque CW. Density of transient K^+ current influences excitability in acutely isolated vasopressin and oxytocin neurones of rat hypothalamus. Journal of Physiology 1998;511:423–432. [PubMed: 9706020]

Foehring RC, Armstrong WE. Pharmacological dissection of high-voltage-activated Ca^{2+} current types in acutely dissociated rat supraoptic magnocellular neurons. Journal of Neurophysiology 1996;76:977–983. [PubMed: 8871212]

Ghamari-Langroudi M, Bourque CW. Flufenamic acid blocks depolarizing after potentials and phasic firing in rat supraoptic neurones. Journal of Physiology 2002;545:537–542. [PubMed: 12456832]

Ghamari-Langroudi M, Bourque CW. Muscarinic receptor modulation of slow after hyperpolarization and phasic firing in rat supraoptic nucleus neurons. Journal of Neuroscience 2004;24:7718–7726. [PubMed: 15342739]

Golding NL, Spruston N. Dendritic sodium spikes are variable triggers of axonal action potentials in hippocampal CA1 pyramidal neurons. Neuron 1998;21:1189–1200. [PubMed: 9856473]

Goldstein SA, Bockenhauer D, O'Kelly I, Zilberberg N. Potassium leak channels and the KCNK family of two-P-domain subunits. Nature Reviews. Neuroscience 2001;2:175–184. 2001.

Greffrath W, Magerl W, Disque-Kaiser U, Martin E, Reuss S, Boehmer G. Contribution of Ca^{2+}-activated K^+ channels to hyperpolarizing after-potentials and discharge pattern in rat supraoptic neurones. Journal of Neuroendocrinology 2004;16:577–588. [PubMed: 15214861]

Greffrath W, Martin E, Reuss S, Boehmer G. Components of after-hyperpolarization in magnocellular neurones of the rat supraoptic nucleus in vitro. Journal of Physiology 1998;513:493–506. [PubMed: 9806998]

Guinamard R, Chatelier A, Demion M, Potreau D, Patri S, Rahmati M, et al. Functional characterization of a Ca^{2+}-activated non-selective cation channel in human atrial cardiomyocytes. Journal of Physiology 2004;558:75–83. [PubMed: 15121803]

Guinamard R, Rahmati M, Lenfant J, Bois P. Characterization of a Ca^{2+}-activated nonselective cation channel during dedifferentiation of cultured rat ventricular cardiomyocytes. Journal of Membrane Biology 2002;188:127–135. [PubMed: 12172638]

Hairer E, Wanner E. Solving ordinary differential equations. II. Stiff and differential-algebraic problems. Springer Series in Computational Mathematics 1996;14:118–130. 565–576.

Han J, Gnatenco C, Sladek CD, Kim D. Background and tandem-pore potassium channels in magnocellular neurosecretory cells of the rat supraoptic nucleus. Journal of Physiology 2003;546:625–639. [PubMed: 12562991]

Hatton GI, Li Z. Mechanisms of neuroendocrine cell excitability. Advances in Experimental Medicine and Biology 1998;449:79–95. [PubMed: 10026788]

Häusser M, Spruston N, Stuart GJ. Diversity and dynamics of dendritic signaling. Science 2000;290:739–744. [PubMed: 11052929]

Hille, B. Ionic channels of excitable membranes. 3. Sunderland, MA: Sinauer; 2001.

Hirasawa M, Mouginot D, Kozoriz MG, Kombian SB, Pittman QJ. Vasopressin differentially modulates non-NMDA receptors in vasopressin and oxytocin neurons in the supraoptic nucleus. Journal of Neuroscience 2003;23:4270–4277. [PubMed: 12764115]

Hoffman DA, Magee JC, Colbert CM, Johnston D. K^+ channel regulation of signal propagation in dendrites of hippocampal pyramidal neurons. Nature 1997;387:869–875. [PubMed: 9202119]

Hoffman NW, Tasker JG, Dudek FE. Immunohistochemical differentiation of electrophysiologically defined neuronal populations in the region of the hypothalamic paraventricular nucleus of the rat. Journal of Comparative Neurology 1991;307:405–416. [PubMed: 1856330]

Johnston D, Hoffman DA, Magee JC, Poolos NP, Watanabe S, Colbert CM, et al. Dendritic potassium channels in hippocampal pyramidal neurons. Journal of Physiology 2000;525:75–81. [PubMed: 10811726]

Joux N, Chevaleyre V, Alonso G, Boissin-Agasse L, Moos FC, Desarmenien MG, et al. High voltage-activated Ca^{2+} currents in rat supraoptic neurones: Biophysical properties and expression of the various channel alpha1 subunits. Journal of Neuroendocrinology 2001;13:638–649. [PubMed: 11442778]

Kang Y, Okada T, Ohmori H. A phenytoin-sensitive cationic current participates in generating the after depolarization and burst after discharge in rat neocortical pyramidal cells. European Journal of Neuroscience 1998;10:1363–1375. [PubMed: 9749790]

Kirkpatrick K, Bourque CW. Activity dependence and functional role of the apamin-sensitive K^+ current in rat supraoptic neurones in vitro. Journal of Physiology 1996;494:389–398. [PubMed: 8841999]

Komendantov AO, Canavier CC. Electrical coupling between model midbrain dopamine neurons: Effect on firing pattern and synchrony. Journal of Neurophysiology 2002;87:1526–1541. [PubMed: 11877524]

Komendantov AO, Komendantova OG, Johnson SW, Canavier CC. A modeling study suggests complementary roles for GABAA and NMDA receptors and the SK channel in regulating the firing pattern in midbrain dopamine neurons. Journal of Neurophysiology 2004;91:346–357. [PubMed: 13679411]

Komendantov, AO.; Trayanova, NA.; Tasker, JG. Roles of intrinsic ionic currents and excitatory synaptic inputs in burst generation in oxytocin-secreting neurons: A computational study (Abstract). Soc. Neurosci. 32nd Annual Meeting; Nov. 2–7, 2002; Orlando, FL. 2002. Program No. 273.4. (Abstract Viewer/Itinerary Planner. Washington, DC: Society for Neuroscience, 2002. CD-ROM).

Komendantov, AO.; Trayanova, NA.; Tasker, JG. Roles of synaptic inputs and retrograde signalling in burst firing in a model of hypothalamic vasopressin neurons (Abstract). Soc. Neurosci. 33rd Annual Meeting; Nov. 8–12, 2003; New Orleans, LA. 2003. Program No. 612.17. (Abstract Viewer/Itinerary Planner. Washington, DC: Society for Neuroscience, 2003. CD-ROM)

Lancaster B, Adams PR. Calcium-dependent current generating the after hyperpolarization of hippocampal neurons. Journal of Neurophysiology 1986;55:1268–1282. [PubMed: 2426421]

Lancaster B, Nicoll RA. Properties of two calcium-activated hyperpolarizations in rat hippocampal neurones. Journal of Physiology 1987;389:187–203. [PubMed: 2445972]

Larkum ME, Rioult MG, Luscher HR. Propagation of action potentials in the dendrites of neurons from rat spinal cord slice cultures. Journal of Neurophysiology 1996;75:154–170. [PubMed: 8822549]

Leonoudakis D, Gray AT, Winegar BD, Kindler CH, Harada M, Taylor DMCR, et al. An open rectifier potassium channel with two pore domains in tandem cloned from rat cerebellum. Journal of Neuroscience 1998;18:868–877. [PubMed: 9437008]

Lesage F, Lazdunski M. Molecular and functional properties of two-pore-domain potassium channels. American Journal of Physiology. Renal Physiology 2000;279:F793–F801. [PubMed: 11053038]

Li Z, Decavel C, Hatton GI. Calbindin-D28k: Role in determining intrinsically generated firing patterns in rat supraoptic neurones. Journal of Physiology 1995;488:601–608. [PubMed: 8576851]

Li Z, Hatton GI. Ca^{2+} release from internal stores: Role in generating depolarizing after-potentials in rat supraoptic neurones. Journal of Physiology 1997a;498:339–350. [PubMed: 9032683]

Li Z, Hatton GI. Reduced outward K^+ conductances generate depolarizing after-potentials in rat supraoptic nucleus neurones. Journal of Physiology 1997b;505:95–106. [PubMed: 9409474]

Liman ER. Regulation by voltage and adenine nucleotides of a Ca^{2+}-activated cation channel from hamster vomeronasal sensory neurons. Journal of Physiology 2003;548:777–787. [PubMed: 12640014]

Luther JA, Halmos KC, Tasker JG. A slow transient potassium current expressed in a subset of neurosecretory neurons of the hypothalamic paraventricular nucleus. Journal of Neurophysiology 2000;84:1814–1825. [PubMed: 11024074]

Luther JA, Tasker JG. Voltage-gated currents distinguish parvocellular from magnocellular neurones in the rat hypothalamic paraventricular nucleus. Journal of Physiology 2000;523:193–209. [PubMed: 10673555]

MacDermott AB, Weight FF. Action potential repolarization may involve a transient, Ca^{2+}-sensitive outward current in a vertebrate neurone. Nature 1982;300:185–188. [PubMed: 6982421]

Magee JC, Johnston D. Characterization of single voltage-gated Na^+ and Ca^{2+} channels in apical dendrites of rat CA1 pyramidal neurons. Journal of Physiology 1995;487:67–90. [PubMed: 7473260]

Mainen, ZF.; Sejnowski, TJ. Methods in neuronal modeling. From ions to networks. 2. Cambridge, MA: MIT Press; 1999. Modeling active dendritic processes in pyramidal neurons; p. 171-209.

Marion NV, Tavalin SJ. Selective activation of Ca^{2+}-activated K^+ channels by co-localized Ca^{2+} channels in hippocampal neurons. Nature 1998;395:900–905. [PubMed: 9804423]

Marty A. Ca^{2+}-dependent K channels with large unitary conductance in chromaffin cell membranes. Nature 1981;291:497–499. [PubMed: 6262657]

Marty A, Neher E. Potassium channels in cultured bovine adrenal chromaffin cells. Journal of Physiology 1985;367:117–141. [PubMed: 2414437]

Mason WT, Leng G. Complex action potential waveform recorded from supraoptic and paraventicular neurons in the rat: Evidence for sodium and calcium spike components at different membrane sites. Experimental Brain Research 1984;56:135–143.

Migliore M, Shepherd GM. Emerging rules for the distributions of active dendritic conductances. Nature Reviews. Neuroscience 2002;3:362–370.

Millhouse, OE. Anatomy of the hypothalamus (Handbook of the hypothalamus. Vol. 1. New York: Marcell Dekker; 1979. A Golgi anatomy of the rodent hypothalamus; p. 221-265.

Oliet SH, Bourque CW. Properties of supraoptic magnocellular neurones isolated from the adult rat. Journal of Physiology 1992;455:291–306. [PubMed: 1362442]

Partridge LD, Muller TH, Swandulla D. Calcium-activated non-selective channels in the nervous system. Brain Research Brain Res Reviews 1994;19:319–325.

Poulain DA, Wakerley JB. Electrophysiology of hypothalamic magnocellular neurones secreting oxytocin and vasopressin. Neuroscience 1982;7:773–808. [PubMed: 6124897]

Poulain DA, Wakerley JB, Dyball RE. Electrophysiological differentiation of oxytocin- and vasopressin-secreting neurones. Proceedings of the Royal Society of London. Series B, Biological Sciences 1977;196:367–384.

Prinz AA, Billimoria CP, Marder E. Alternative to hand-tuning conductance-based models: Construction and analysis of databases of model neurons. Journal of Neurophysiology 2003;90:3998–4015. [PubMed: 12944532]

Randle JC, Bourque CW, Renaud LP. Serial reconstruction of Lucifer yellow-labeled supraoptic nucleus neurons in perfused rat hypothalamic explants. Neuroscience 1986;17:453–467. [PubMed: 3703246]

Roper P, Callaway J, Armstrong W. Burst initiation and termination in phasic vasopressin cells of the rat supraoptic nucleus: A combined mathematical, electrical, and calcium fluorescence study. Journal of Neuroscience 2004;24:4818–4831. [PubMed: 15152042]

Roper P, Callaway J, Shevchenko T, Teruyama R, Armstrong W. AHP's, HAP's and DAP's: How potassium currents regulate the excitability of rat supraoptic neurones. Journal of Computational Neuroscience 2003;15:367–389. [PubMed: 14618071]

Sah P, Bekkers JM. Apical dendritic location of slow after hyperpolarization current in hippocampal pyramidal neurons: Implications for the integration of long-term potentiation. Journal of Neuroscience 1996;16:4537–4542. [PubMed: 8764642]

Sah P, Davies P. Calcium-activated potassium currents in mammalian neurons. Clinical and Experimental Pharmacology and Physiology 2000;27:657–663. [PubMed: 10972528]

Siemen D. Nonselective cation channels. EXS 1993;66:3–25. [PubMed: 7505661]

Stern JE, Armstrong WE. Electrophysiological differences between oxytocin and vasopressin neurones recorded from female rats in vitro. Journal of Physiology 1995;488:701–708. [PubMed: 8576859]

Stern JE, Armstrong WE. Changes in the electrical properties of supraoptic nucleus oxytocin and vasopressin neurons during lactation. Journal of Neuroscience 1996;16:4861–4871. [PubMed: 8756418]

Stern JE, Armstrong WE. Sustained outward rectification of oxytocinergic neurones in the rat supraoptic nucleus: Ionic dependence and pharmacology. Journal of Physiology 1997;500:497–508. [PubMed: 9147333]

Stern JE, Armstrong WE. Reorganization of the dendritic trees of oxytocin and vasopressin neurons of the rat supraoptic nucleus during lactation. Journal of Neuroscience 1998;18:841–853. [PubMed: 9437006]

Stuart GJ, Sakmann B. Active propagation of somatic action potentials into neocortical pyramidal cell dendrites. Nature 1994;367:69–72. [PubMed: 8107777]

Sun X, Gu XQ, Haddad GG. Calcium influx via Land N-type calcium channels activates a transient large-conductance Ca^{2+}-activated K^{+} current in mouse neocortical pyramidal neurons. Journal of Neuroscience 2003;23:3639–3648. [PubMed: 12736335]

Tanaka M, Cummins TR, Ishikawa K, Black JA, Ibata Y, Waxman SG. Molecular and functional remodeling of electrogenic membrane of hypothalamic neurons in response to changes in their input. Proceedings of the National Academy of Sciences of the United States of America 1999;96:1088–1093. [PubMed: 9927698]

Tasker JG, Dudek FE. Electrophysiological properties of neurones in the region of the paraventricular nucleus in slices of rat hypothalamus. Journal of Physiology 1991;434:271–293. [PubMed: 2023120]

Teruyama R, Armstrong WE. Changes in the active membrane properties of rat supraoptic neurones during pregnancy and lactation. Journal of Neuroendocrinology 2002;14:933–944. [PubMed: 12472874]

Teruyama, R.; Armstrong, WE. Characterization of the fast depolarizing after-potential in vasopressin neurons in the supraoptic nucleus (Abstract). Soc. Neurosci. 36th Annual Meeting; Oct. 14–18, 2006; Atlanta, GA. 2006. Program No. 153.8. (Abstract Viewer/Itinerary Planner. Washington, DC: Society for Neuroscience, 2006. CD-ROM).

Teulon, J. Ca^{2+}-activated non-selective cation channels. In: Endo, M.; Kurachi, Y.; Mishina, M., editors. Pharmacology of ionic channel function: Activators and inhibitors. Berlin: Springer; 2000. p. 625-649.

Thorn P, Petersen OH. Nonselective cation channels in exocrine gland cells. EXS 1993;66:185–200. [PubMed: 7505650]

Vergara C, Latorre R, Marrion NV, Adelman JP. Calcium-activated potassium channels. Current Opinion in Neurobiology 1998;8:321–329. [PubMed: 9687354]

Vogalis F, Harvey JR, Lohman RJ, Furness JB. Action potential after depolarization mediated by a Ca^{2+}-activated cation conductance in myenteric AH neurons. Neuroscience 2002;115:375–393. [PubMed: 12421604]

Wakerley JB, Lincoln DW. The milk-ejection reflex of the rat: A 20- to 40-fold acceleration in the firing of paraventricular neurones during oxytocin release. Journal of Endocrinology 1973;57:477–493. [PubMed: 4577217]

Widmer H, Boissin-Agasse L, Richard P, Desarmenien MG. Differential distribution of a potassium current in immunocytochemically identified supraoptic magnocellular neurones of the rat. Neuroendocrinology 1997;65:229–237. [PubMed: 9142994]

Wilson CJ, Callaway JC. Coupled oscillator model of the dopaminergic neuron of the substantia nigra. Journal of Neurophysiology 2000;83:3084–3100. [PubMed: 10805703]

Womack MD, Khodakhah K. Characterization of large conductance Ca^{2+}-activated K^{+} channels in cerebellar Purkinje neurons. European Journal of Neuroscience 2002;16:1214–1222. [PubMed: 12405981]

Xia XM, Fakler B, Rivard A, Wayman G, Johnson-Pais T, Keen JE, et al. Mechanisms of calcium gating in small-conductance calcium-activated potassium channels. Nature 1998;395:503–507. [PubMed: 9774106]

Zhu ZT, Munhall A, Shen KZ, Johnson SW. Calcium-dependent subthreshold oscillations determine bursting activity induced by N-methyl-D-aspartate in rat subthalamic neurons in vitro. European Journal of Neuroscience 2004;19:1296–1304. [PubMed: 15016087]

Appendix

The membrane potential of each compartment of the magnocellular neuron is described by the current balance equation:

$$\begin{aligned} C_m(\mathrm{d}V_{\mathrm{sd}}/\mathrm{d}t) &= I_{\mathrm{Na,sd}} + I_{A,\mathrm{sd}} + I_{K(DR),\mathrm{sd}} + I_{\mathrm{Ca},L,\mathrm{sd}} \\ &\quad + I_{\mathrm{CAN,sd}} + I_{\mathrm{SK,sd}} + I_{L,\mathrm{sd}} + I_{\mathrm{sd}-pd} \\ C_m(\mathrm{d}V_{\mathrm{pd}}/\mathrm{d}t) &= I_{\mathrm{Na,pd}} + I_{A,\mathrm{pd}} + I_{K(DR),\mathrm{pd}} + I_{\mathrm{Ca},L,\mathrm{pd}} + I_{\mathrm{Ca},N,\mathrm{pd}} \\ &\quad + I_{\mathrm{SK,pd}} + I_{\mathrm{BK,pd}} + I_{\mathrm{CAN,pd}} + I_{L,\mathrm{pd}} + I_{\mathrm{pd}-\mathrm{s}} \\ &\quad + I_{\mathrm{pd}-\mathrm{sd}} \\ C_m(\mathrm{d}V_{\mathrm{s}}/\mathrm{d}t) &= I_{\mathrm{Na,s}} + I_{A,s} + I_{K(DR),\mathrm{s}} + I_{\mathrm{Ca},L,\mathrm{s}} + I_{\mathrm{Ca},N,\mathrm{s}} + I_{\mathrm{SK,s}} \\ &\quad + I_{\mathrm{BK,s}} + I_{\mathrm{CAN,s}} + I_{L,\mathrm{s}} + I_{\mathrm{s}-\mathrm{pd}} + I_{\mathrm{stim}}, \end{aligned}$$

where C_m is the specific neuronal membrane capacitance; $I_{\mathrm{sd\text{-}pd}}$, $I_{\mathrm{pd\text{-}s}}$, $I_{\mathrm{pd\text{-}sd}}$, and $I_{\mathrm{s\text{-}pd}}$ are the intercompartmental coupling currents; and I_{stim} is the applied microelectrode current. The subscripts “sd,” “pd,” and “s” indicate secondary (distal) dendritic compartment, primary (proximal) dendritic compartment, and somatic compartment, respectively. Each compartment has its own set of conductances for the ion currents.

A.1 Membrane ion currents

The membrane ion currents in the model were described using the Hodgkin-Huxley formalism. The subscript “*i*” indicates a compartment (s, pd or sd).

A.1.1 Transient sodium current (based on Tanaka et al. 1999)

$$\begin{aligned} I_{\mathrm{Na},i} &= g_{\mathrm{Na},i} m_{\infty}^3 i h_i (V_i - E_{\mathrm{Na}}); \\ m_{\infty,i} &= 1/(1+\exp(-(V_i+34.6)/6.2)); \\ \mathrm{d}h_i/\mathrm{d}t &= (h_{\infty,i} - h_i)/\tau_{h,i}; \\ h_{\infty,i} &= 1/(1+\exp((V_i+61.6)/6.8)); \\ \tau_{h,i} &= 26.0/(1+\exp((V_i+46.0)/7.0)) \\ &\quad +3.0/(1+\exp((V_i+49.0)/20.0))+0.1. \end{aligned}$$

A.1.2 Calcium currents (based on Joux et al. 2001)

A.1.2.1 High threshold current with no or very slow inactivation (N-type)

$$\begin{aligned} I_{\mathrm{Ca},N,i} &= g_{\mathrm{Ca},N,i} m_{N,i} (V_i - E_{\mathrm{Ca},i}); \\ \mathrm{d}m_{N,i}/\mathrm{d}t &= (m_{N\infty,i} - m_{N,i})/t_{\mathrm{mN}}; \\ m_{N\infty,i} &= 1.0/(1.0+\exp(-(V_i+11.0)/4.2)). \end{aligned}$$

A.1.2.2 Lower threshold (L-type) current

$$I_{\mathrm{Ca},L,i}=g_{\mathrm{Ca},L,i}\,m_{L,ih}L_{\infty,i}(V_i-E_{\mathrm{Ca},i});$$
$$\mathrm{d}m_{L,i}/\mathrm{d}t=(m_{L\infty,i}-m_{L,i})/\tau_{mL};$$
$$m_{L\infty,s}=0.5/(1.0+\exp(-(V_s+27.0)/4.5))+0.5/(1.0+\exp(-(V_s+11.4)/2.0));$$
$$m_{L\infty,\mathrm{pd}}=0.4/(1.0+\exp(-(V_{\mathrm{pd}}+27.0)/4.5))+0.6/(1.0+\exp(-(V_{\mathrm{pd}}+11.4)/2.0));$$
$$m_{L\infty,\mathrm{sd}}=0.3/(1.0+\exp(-(V_{\mathrm{sd}}+27.0)/4.5))+0.7/(1.0+\exp(-(V_{\mathrm{sd}}+11.4)/2.0));$$
$$h_{L\infty,i}=0.2\,K_{M,L1}^4/\left(K_{M,L1}^4+[\mathrm{Ca}^{2+}]_{\mathrm{in},i}^4\right)+0.8\,K_{M,L2}/\left(K_{M,L2}+[\mathrm{Ca}^{2+}]_{\mathrm{in},i}\right).$$

A.1.3 Potassium currents

A.1.3.1 Delayed rectifier current (based on Luther and Tasker 2000)

$$I_{KDR,i}=g_{KDR,i}n^3i(V_i-E_K);$$
$$\mathrm{d}n_i/\mathrm{d}t=(n_{\infty,i}-n_i)/\tau_n;$$
$$n_{\infty,i}=1/(1+\exp(-(V_i+18.3)/9));$$
$$\tau_{n,i}=3.6/(1+\exp((V_i-3.0)/5.0))+1.6/(1+\exp(V_i/10.0))+5.2/(1+\exp(-(V_i+65.0)/6.0))-4.0.$$

A.1.3.2 A-current (based on Luther and Tasker 2000)

$$I_{A,i}=g_{A,i}p_i^4q_i(V_i-E_K);$$
$$\mathrm{d}p_i/\mathrm{d}t=(p_{\infty,i}-p_i)/\tau_{p,i};$$
$$p_{\infty,i}=1/(1+\exp(-(V_i+46.8)/9.3));$$
$$\mathrm{d}q_i/\mathrm{d}t=(q_{\infty,i}-q_i)/\tau_{q,i};$$
$$q_{\infty,i}=1/(1+\exp((V_i+80.1)/8.8));$$
$$\tau_{p,i}=0.2+6.4/(\exp((V_i+68.0)/27.0))+4.0\exp(-(V_i+130.0)/35.0)+0.4/(1+\exp((V_i-25.0)/4.0));$$
$$\tau_{q,i}=350/(1+\exp((V_i+120)/10.0))+7.5/(1+\exp((V_i+8.0)/5.0))+12.5/(1+\exp((V_i-2.0)/5.0))+1.0.$$

A.1.3.3 SOR current (for the model OT neuron only; based on Stern and Armstrong 1995)

$$I_{\mathrm{SOR},i}=g_{\mathrm{SOR},i}m_{\mathrm{SOR},i}(V_i-E_K);$$
$$\mathrm{d}m_{\mathrm{SOR},i}/\mathrm{d}t=(m_{\mathrm{SOR}\infty,i}-m_{\mathrm{SOR},i})/\tau_{m,\mathrm{SOR}};$$
$$m_{\mathrm{SOR}\infty,i}=1.0/(1.0+\exp(-(V_i+60.0)/4.0)).$$

A.1.3.4 Ca^{2+}-sensitive K^+ currents (In the equations, $[Ca^{2+}]$ is in mM)

A.1.3.4.1 SK current (based on Vergara et al. 1998; Xia et al. 1998)

$$I_{SK,i}=g_{,SK,i}m_{SK\infty,i}(V_i-E_K);$$
$$m_{SK\infty,i}=1/\left(1+\left(K_{m,SK}/[Ca^{2+}]_{in,i}\right)^{4.5}\right).$$

A.1.3.4.2 BK current (based on Dopico et al. 1999)

$$I_{BK,i}=g_{BK,i}m_{BK\infty,i}(V_i-E_K);$$
$$m_{BK\infty,i}=1/(1+\exp(-(V_i-(-138.37\log_{10}([Ca^{2+}]_{BK,i})-463))/11)).$$

A.1.4 CAN current

$$I_{CAN,i}=g_{CAN,i}m_{CAN,i}(2V_i-E_{Na}-E_K);$$
$$m_{CAN,i}=A_i([Ca^{2+}]_{in,i})\cdot B_i(V_i,[Ca^{2+}]_{in,i});$$
$$A_i([Ca^{2+}]_{in,i})=([Ca^{2+}]_{in,i})^2/(([Ca^{2+}]_{in,i})^2+K^2_{d,CAN});$$
$$B_i(V_i,[Ca^{2+}]_{in,i})=1/(1+\exp(-(V_i-V_{CAN,h}\cdot S_i([Ca^{2+}]_{in,i}))/3));$$
$$S_i=1.0/(1+\exp(([Ca^{2+}]_{in,i}-a_1)/b_1))+1.2/(1+\exp(([Ca^{2+}]_{in,i}-a_2)/b_2))-5.9.$$

A.1.5 Linear leakage current

$$I_{L,i}=I_{L,Na,i}+I_{L,K,i};\quad I_{L,K,i}=g_{L,K,i}(V_i-E_K);$$
$$I_{L,Na,i}=g_{L,Na,i}(V_i-E_{Na})$$

A.2 Calcium dynamics

A.2.1 Calcium dynamics in the cytoplasm

$$d[Ca^{2+}]_i/dt=2f_{Ca}\left(-(\sum I_{Ca,j,i})/(d_iF)-U_i\left([Ca^{2+}]_i-[Ca^{2+}]_r\right)\right)$$

Subscript "*j*" represents the L- or N-type Ca^{2+} current in the compartment.

A.2.2 Calcium dynamics in the BK channel subdomains

$$d\left[Ca^{2+}\right]_{BK,i}/dt=2f_{Ca,BK}\left(-I_{Ca,N,j}/(rd_iF)-K_{BK,i}\left([Ca^{2+}]_{BK,i}-[Ca^{2+}]_r\right)\right),$$

Here, "i" can be either "s" (soma) or "pd" (primary dendrite).

A.3 Intercompartmental coupling currents

$$
\begin{gathered}
I_{\mathrm{sd-pd}}=g_{\mathrm{sd-pd}}(V_{\mathrm{sd}}-V_{\mathrm{pd}});\\
I_{\mathrm{pd-sd}}=g_{\mathrm{pd}}(V_{\mathrm{pd}}-V_{\mathrm{sd}});\\
I_{\mathrm{pd-s}}=g_{\mathrm{pd-s}}(V_{\mathrm{pd}}-V_{\mathrm{s}});\\
I_{\mathrm{s-pd}}=g_{\mathrm{s-pd}}(V_{\mathrm{s}}-V_{\mathrm{pd}});\\
G_{\mathrm{s-pd}}=10^2\pi d_{\mathrm{pd}}^2 d_{\mathrm{s}}^2/2\,Ra\left(L_{\mathrm{pd}}\mathrm{d}_{\mathrm{s}}^2+L_{\mathrm{s}}\mathrm{d}_{\mathrm{pd}}^2\right);\\
G_{\mathrm{pd-sd}}=10^2\pi\mathrm{d}_{\mathrm{pd}}^2\mathrm{d}_{\mathrm{sd}}^2/2\,Ra\left(L_{\mathrm{pd}}\mathrm{d}_{\mathrm{sd}}^2+L_{\mathrm{sd}}\mathrm{d}_{\mathrm{pd}}^2\right);\\
g_{\mathrm{s-pd}}=2\cdot 10^8\,G_{\mathrm{s-pd}}/(\pi\mathrm{d}_{\mathrm{s}}L_{\mathrm{s}});\\
g_{\mathrm{pd-s}}=10^8\,G_{\mathrm{s-pd}}/(\pi\mathrm{d}_{\mathrm{pd}}L_{\mathrm{pd}});\\
g_{\mathrm{pd-sd}}=4\cdot 10^8\,G_{\mathrm{pd-sd}}/(\pi\mathrm{d}_{\mathrm{pd}}L_{\mathrm{pd}});\\
g_{\mathrm{sd-pd}}=10^8\,G_{\mathrm{pd-sd}}/(\pi\mathrm{d}_{\mathrm{sd}}L_{\mathrm{sd}}).
\end{gathered}
$$

A.4 Applied current

$$I_{\mathrm{stim}}=I_{\mathrm{ST}}/(p\mathrm{d}_{\mathrm{s}}L_{\mathrm{s}}).$$

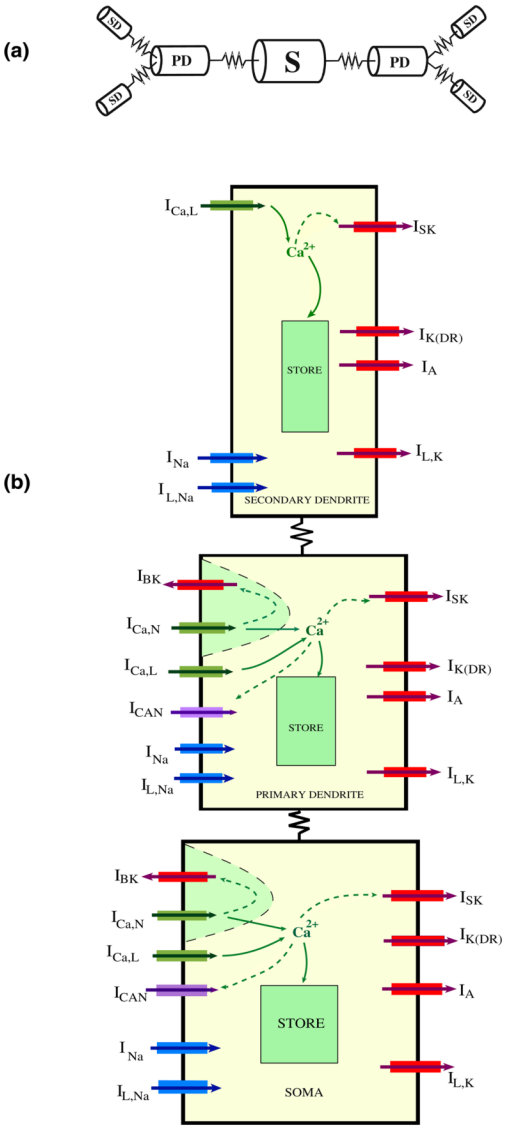

Fig. 1.

Compartmental structure of the magnocellular neuron model. (**a**) The seven-compartment model of magnocellular neurons. The model features a cylindrical somatic compartment (S) and two symmetrical dendrites, each subdivided into a single cylindrical primary dendritic compartment (PD) and two cylindrical secondary dendritic compartments (SD). (**b**) Compartmental ionic currents and calcium dynamics. Only one primary dendrite and one secondary dendrite are shown for simplicity. I_{Na} denotes voltage-gated transient sodium current; $I_{L,Na}$ sodium leak, $I_{K(DR)}$ potassium delayed rectifier current, I_A A-type potassium current, $I_{L,K}$ potassium leak, I_{SK} apamin-sensitive Ca^{2+} activated K^+ current mediated by small-conductance K^+ (SK) channels and underlying the AHP, I_{BK} Ca^{2+}-activated K^+ current mediated by large conductance K^+ (BK) channels, $I_{Ca,N}$ N-type calcium current, $I_{Ca,L}$ L-type calcium current, I_{CAN} Ca^{2+}-dependent non-selective cation current underlying the DAP

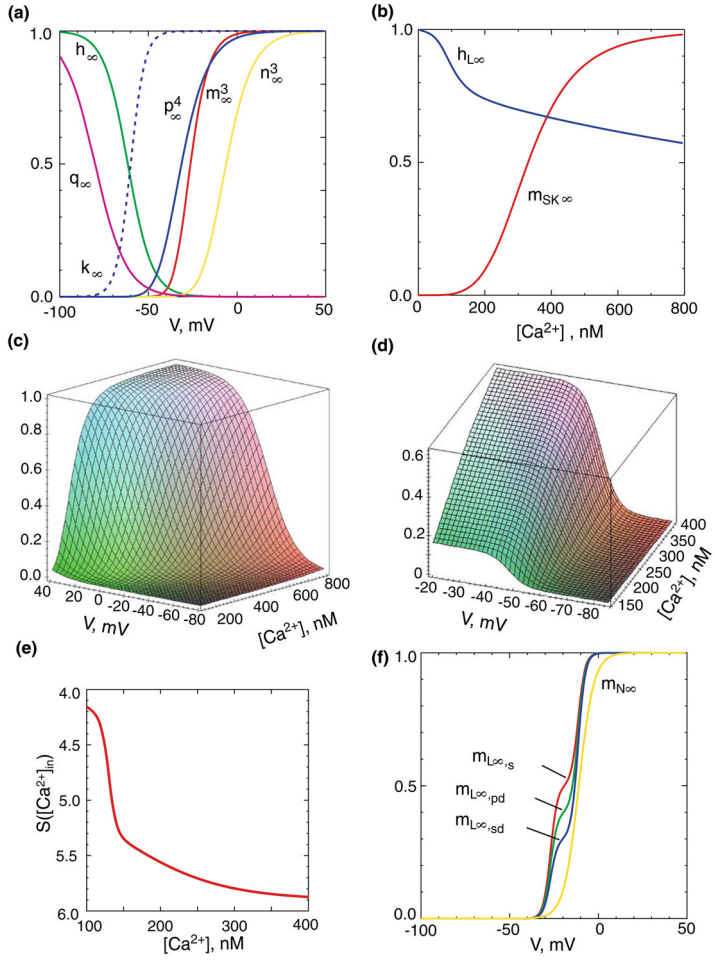

Fig. 2.

Steady-state characteristics of activation and inactivation of ionic currents in the model. (**a**) Steady-state characteristics of voltage-gated Na^+ and K^+ currents. The variables m_∞^3 (*red*) and h_∞ (*green*) are associated with I_{Na}, n_∞^3 (yellow) with $I_{K(DR)}$, p_∞^4 (*blue*) and q_∞ (*magenta*) with I_A, and k_∞ (*blue dashed line*) with I_{SOR}. (**b**) Steady-state activation of SK ($m_{SK\infty}$) current (*red*) and inactivation of the L-type current (*blue*) as functions of intracellular $[Ca^{2+}]$. (**c**) Steady-state activation ($m_{BK\infty}$) of the BK current as a function of voltage and intracellular $[Ca^{2+}]$. (**d**) Steady-state activation of the CAN current $m_{CAN\infty}$ as a function of voltage and intracellular $[Ca^{2+}]$. The activation function provides residual spike-induced inward after-current under blockade of Ca^{2+} influx (see Bourque 1986). (**e**) Ca^{2+}-sensitive shift of half-activation potential of CAN current. (**f**) Steady-state characteristics for activation of L- and N-type Ca^{2+} currents in the different compartments. *Red, green and blue lines* show characteristics of L-type current activation in the soma, primary dendrites and secondary dendrites, respectively; *yellow line* shows the characteristics of N-type current

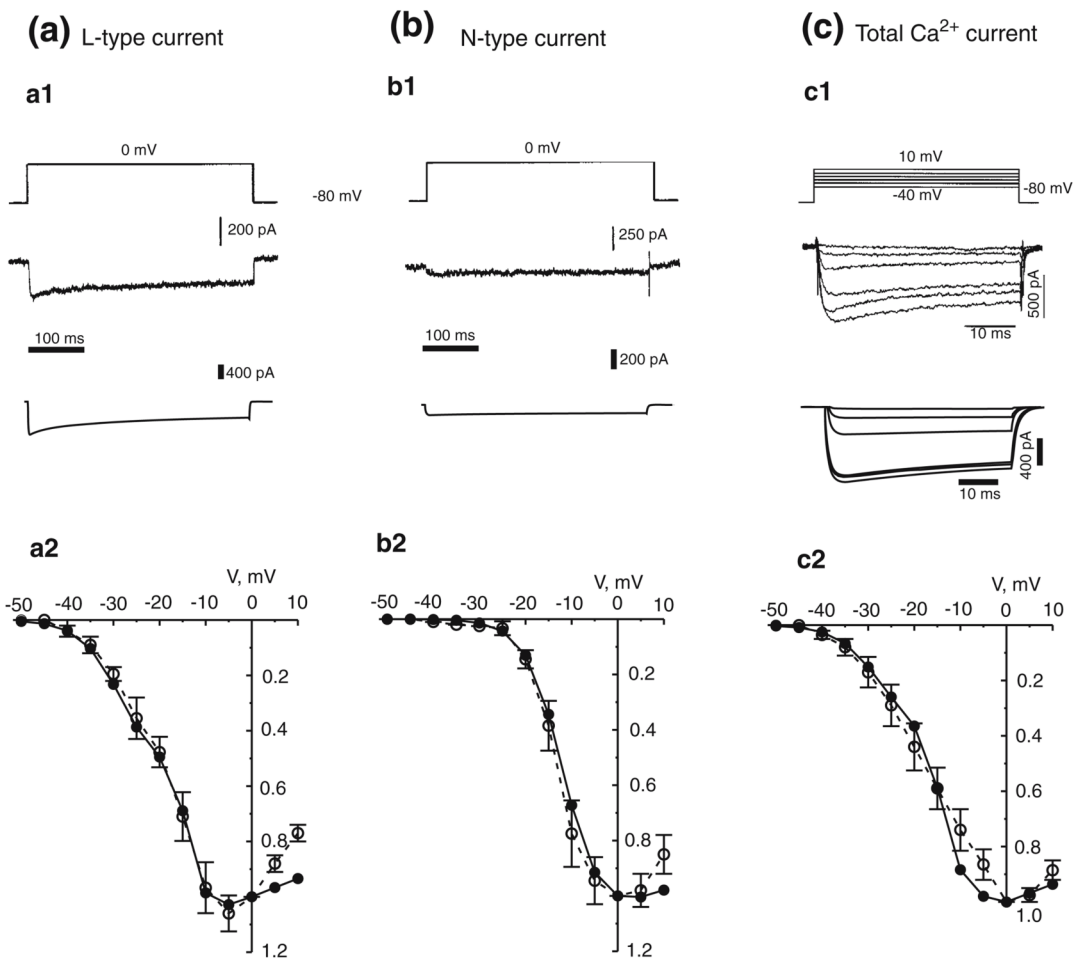

Fig. 3.

Ca^{2+} currents in the model and in rat MNCs. (**a**) L-type current. (**b**) N-type current. (**c**) Total Ca^{2+} current. *a1*, *b1* and *c1* show L-type, N-type and total Ca^{2+} current responses, respectively, to a depolarizing step from −80 to 0 mV (*a1*, *b1*) or to six depolarizing steps in 5-mV increasing increments from −40 to −10 mV from a holding potential of −80 mV (*c1*) (*top panels*) in MNCs recorded experimentally in the SON (*middle panels*, modified from Joux et al. 2001) and in the model (*bottom panels*). *a2*, *b2* and *c2* show current-voltage relationships for the L-type, N-type and total Ca^{2+} currents, respectively. Current values are normalized to the currents evoked at 0 mV. Current-voltage curves for the L-type currents were fitted with a double Boltzmann function, and for the N-type current with a single Boltzmann function. *Empty circles* and *dotted lines* correspond to the experimental data (taken from Joux et al. 2001), *filled circles* and *solid lines* correspond to the model currents

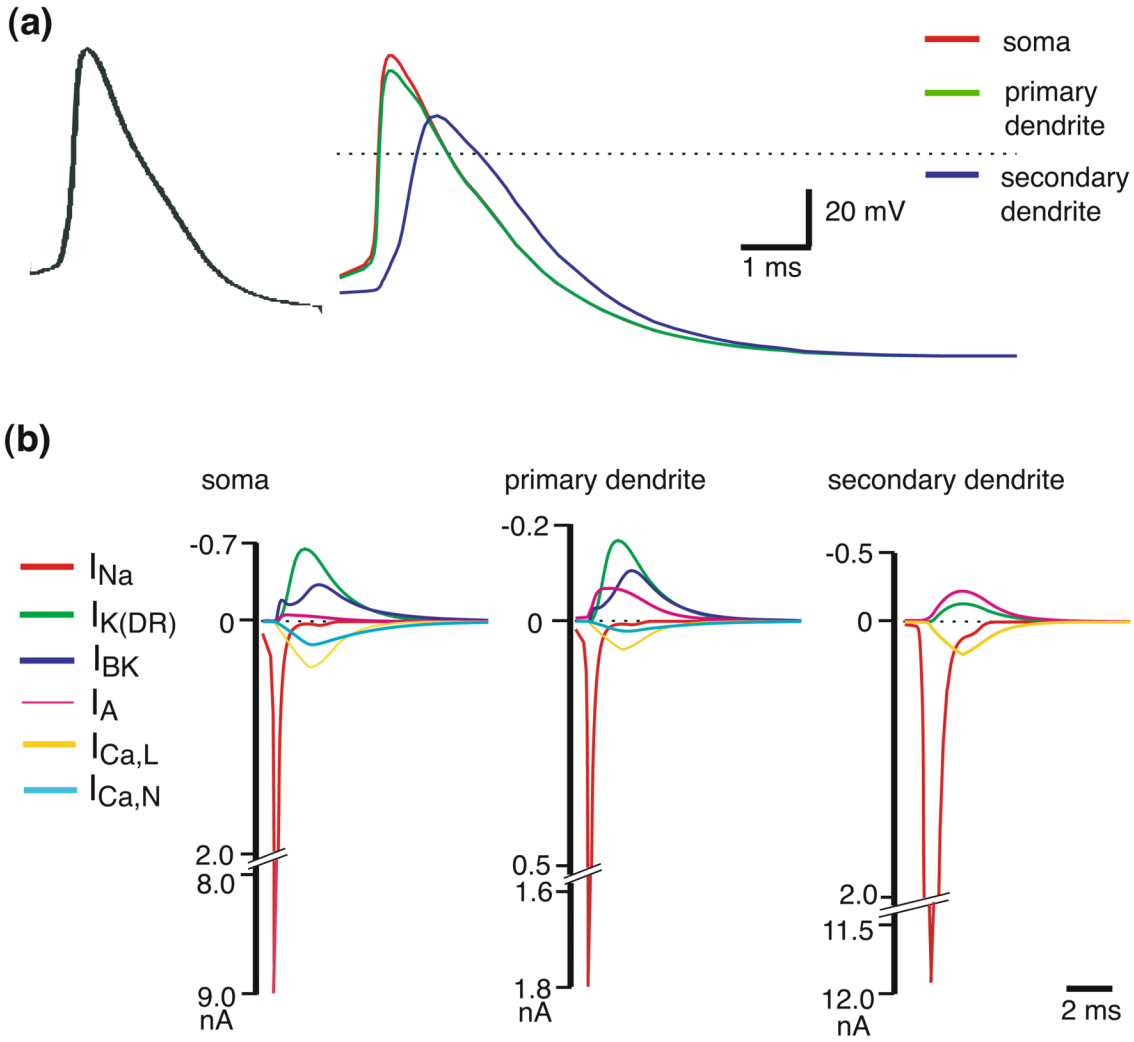

Fig. 4.

Simulation of voltage-gated currents and action potentials in different compartments of the MNC model. (**a**) A single action potential evoked by somatic injection of a suprathreshold depolarizing current and recorded in the soma of a rat SON MNC in a hypothalamic slice (*left panel*, see Luther and Tasker 2000 for methods) and in the soma, primary dendrite and secondary dendrite of the model MNC (*right panel*). The action potential recorded in the secondary dendrite (*blue trace*) was delayed compared to the action potential recorded in the soma (*red trace*) and in the primary dendrite (*green trace*) of the model. *Dashed line* indicates 0 mV. (**b**) Development of ionic currents in the different compartments during the spike depicted in *a*. The figure shows transient sodium currents (I_{NA}, *red*), delayed rectifier potassium currents ($I_{K(DR)}$, *green*), voltage- and Ca^{2+}-activated potassium (BK) currents (I_{BK}, *blue*), A currents (I_A, *pink*), and L- and N- type Ca^{2+}-currents ($I_{Ca,L}$, *yellow*, and $I_{Ca,N}$, *light blue*, respectively) generated in the model's soma (*left*), primary dendrite (*middle*) and secondary dendrite (*right*)

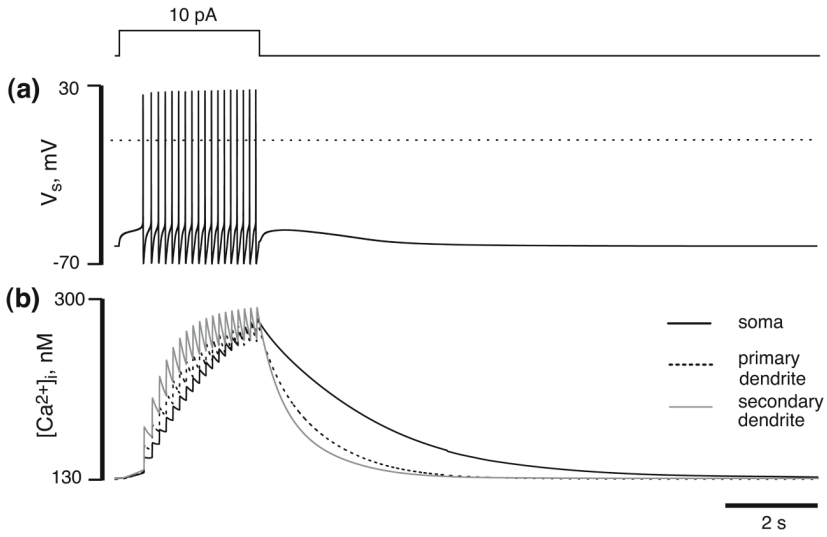

Fig. 5.

Time course of changes in calcium concentration and membrane potential in the model MNC. Somatic potential (V_S) was −59 mV and a depolarizing current injection of 10 pA was applied as shown in the top trace. (**a**) Time course of the change in membrane potential in the soma. *Dashed line* indicates 0 mV. (**b**) Time course of changes in intracellular [Ca^{2+}] in the different compartments, corresponding to the activity shown in *A*

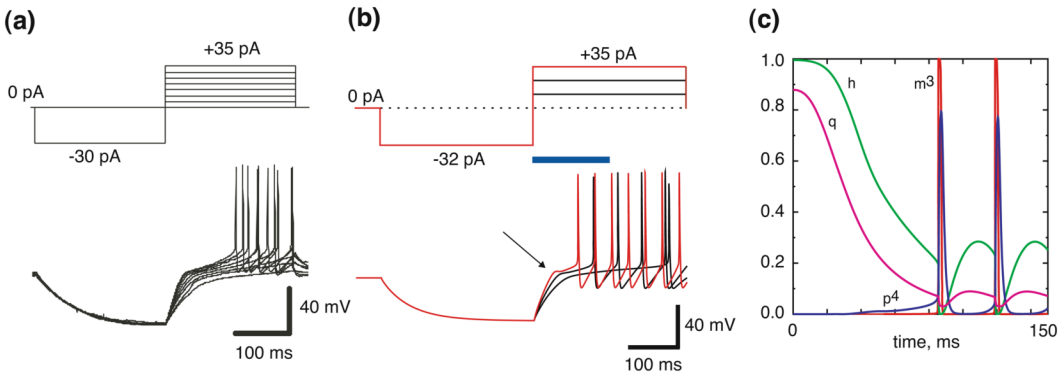

Fig. 6.

Simulation of transient outward rectification (TOR) in the model MNC. (**a**) Experimental record of the membrane responses of an MNC in the PVN to a series of incrementally larger depolarizing current pulses (*top traces*) following steady-state hyperpolarization from resting potential. The TOR is elicited with stronger depolarization (modified from Luther and Tasker 2000). (**b**) Simulated membrane response, including TOR (*arrow*), in the model neuron elicited by the stimulation protocol presented in the top traces. *Blue bar* corresponds to the 150 ms time span represented in *c*. (**c**) Time course of the gating variables for I_{Na} (m^3 and h) and I_A (p^4 and q) that correspond to the development of TOR presented in the *red trace* in *c*

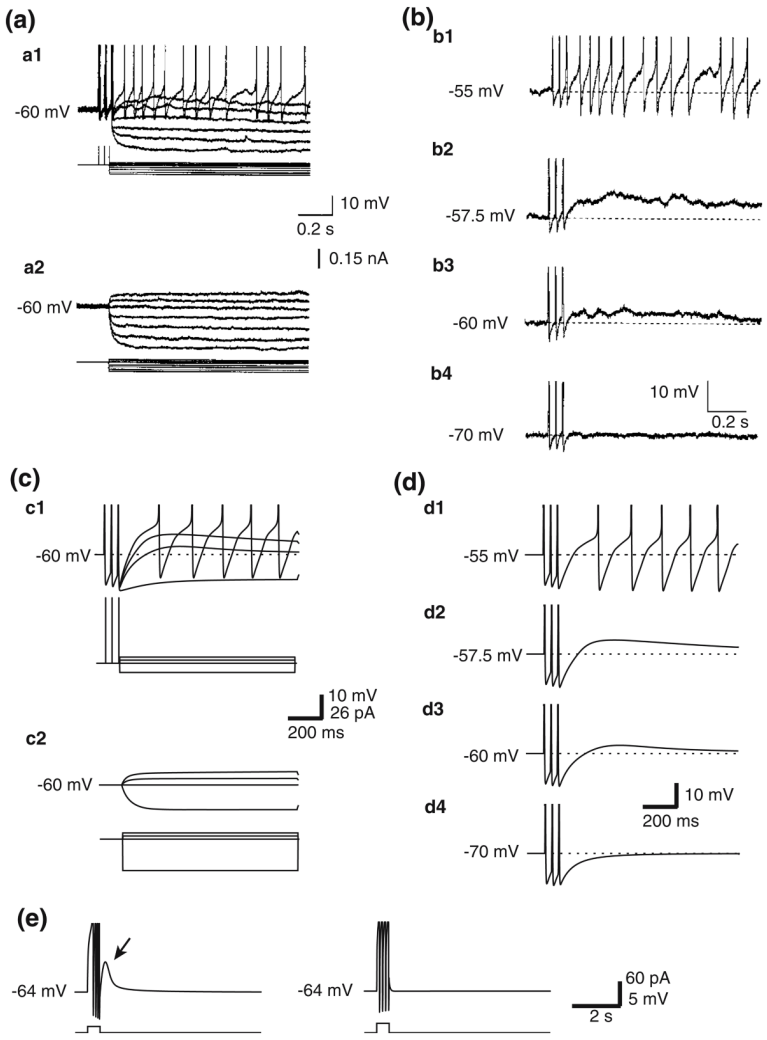

Fig. 7.

Voltage dependence of the DAP in MNCs. (**a**) In vitro brain slice recording of a SON MNC (from Li and Hatton 1997a). (*a1*) Immediately following a train of three spikes elicited by successive current injections the membrane potential was brought to various levels in order to examine voltage dependence of the DAP. (*a2*) The same protocol as in *a1* except without the current pulses to elicit conditioning spikes. The traces below the voltage records indicate the times that current pulses were applied; action potentials are enlarged and truncated to display DAPs. (**b**) Traces obtained from a real MNC by subtracting voltage responses in *a2* from those shown in *a1* (from Li and Hatton 1997a). The DAP is not seen at a membrane potential of −70 mV (*b4*), appears at −60 mV, and increases in size with membrane depolarization (*b1*,*b2*) until it reaches spike threshold and is masked by repetitive spiking activity (*b1*). In all figures, interrupted lines indicate the membrane potentials shown; the traces below the voltage records indicate the times that current pulses were applied; action potentials are enlarged and truncated to display DAPs. (**c**) Simulations using a protocol similar to that shown in the in in vitro brain slice recording in *a*. The membrane potential was brought to levels −70, −60, −57.5, and −55 mV. Current pulses (177 pA) and spikes are truncated. (**d**) Traces obtained by subtracting simulated voltage responses in *c2* from those shown in *c1*, similar to the protocol used in the experiments and shown in *b*. *Dotted lines* indicate 0 mV; values −55, −57.5, −60 and −70 mV indicate levels of holding membrane potential. (**e**) *Left panel*—A DAP (*arrow*) was elicited in

the model MNC following four spikes evoked by a depolarizing current pulse. The AHP was blocked by setting g_{SK} to zero. *Right panel*—simulated blockade of the DAP by setting g_{CAN} to zero (*Cf.* experimental blockade of the DAP by flufenamic acid in Ghamari-Langroudi and Bourque (2002)). Spikes are truncated

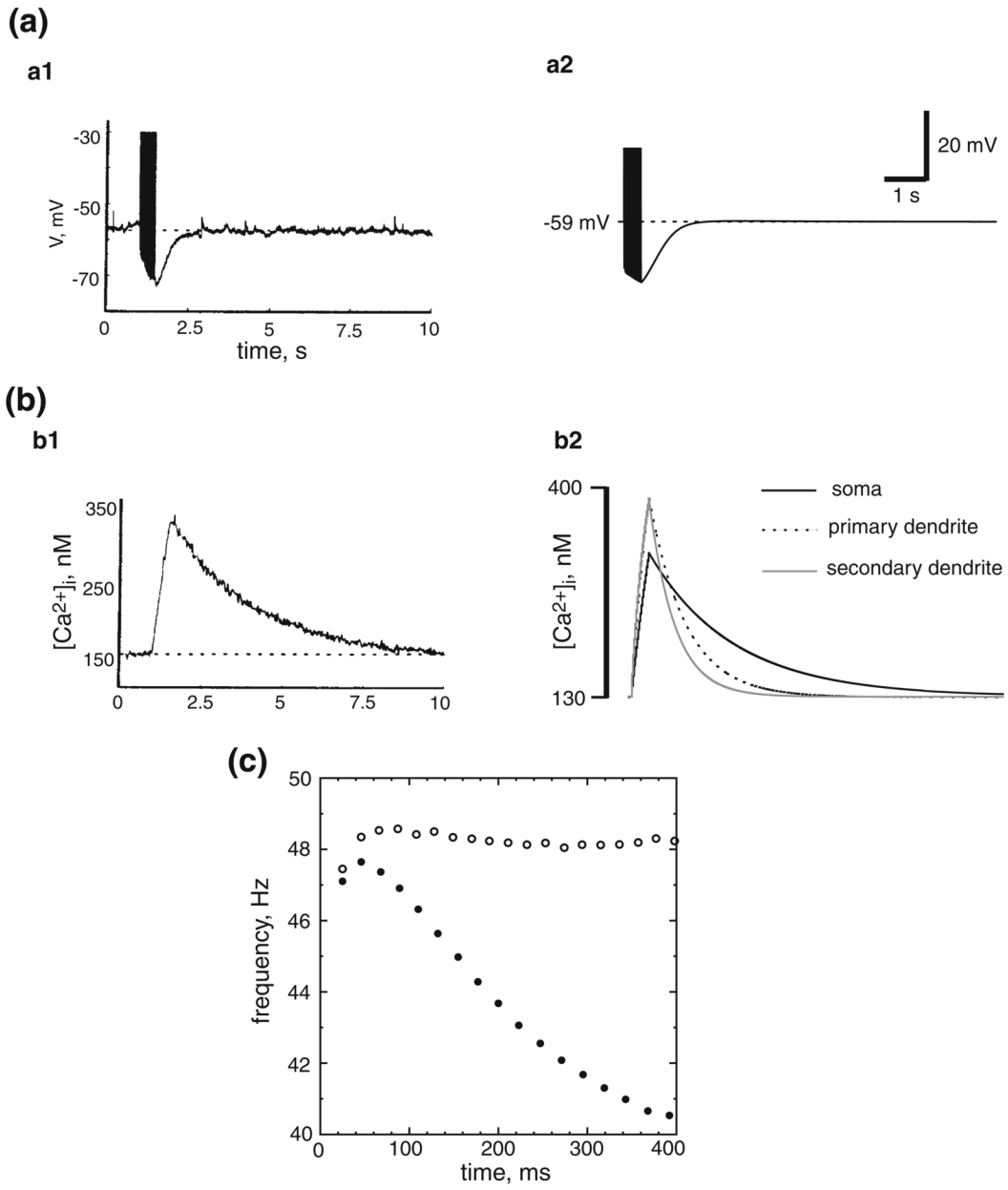

Fig. 8.

AHP and spike frequency adaptation in the model MNC. (**a**) A spike train and subsequent AHP elicited by repetitive stimulation (5 ms pulses at 40 Hz for 1 s) in a somatic recording of a MNC (*a1*) (modified from Roper et al. 2003) and in the soma of the model MNC (*a2*). Action potentials are truncated. (**b**) Ca^{2+} dynamics in the soma of the recorded MNC (*b1*) (modified from Roper et al. 2003) and in the different compartments of the model MNC (*b2*) under the same stimulation protocol as in (**a**). (**c**) Spike frequency adaptation during spike trains evoked in the model by a current pulse of 67 pA. Instantaneous spike frequency within the train in control (*filled circles*) and with a 60% blockade of g_{SK} (*open circles*). The values of $g_{SK,s}$=10 μS/cm^2, $g_{SK,pd}$ =40 μS/cm^2, $g_{SK,sd}$=25 μS/cm^2 provided an AHP waveform and somatic [Ca^{2+}] transient that most closely matched experimental data

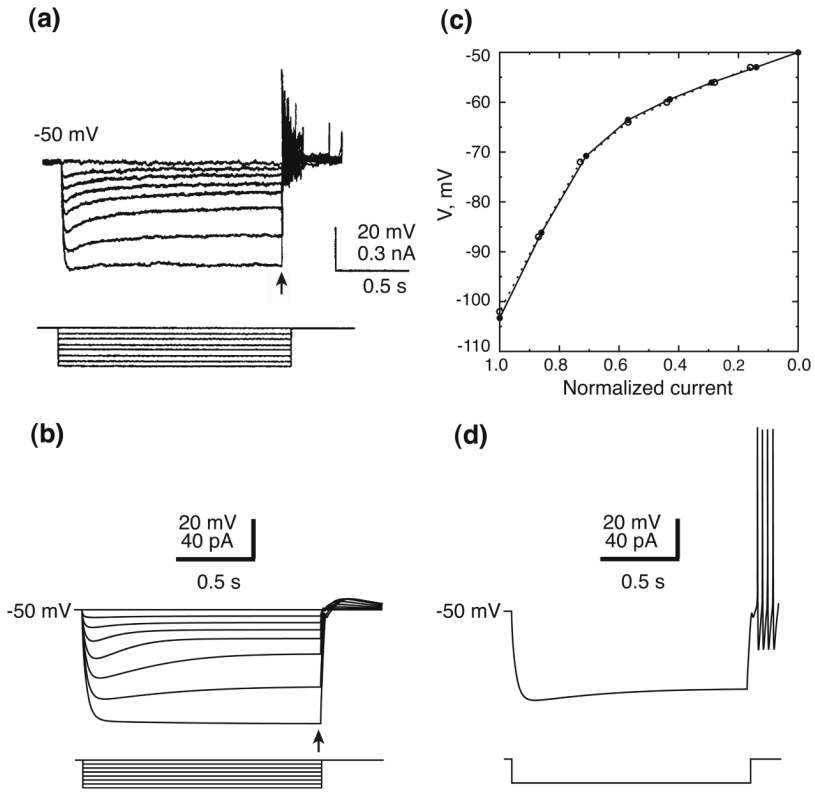

Fig. 9.

SOR generation in the model MNC. (**a**) Voltage responses to hyperpolarizing current pulses from a subthreshold depolarized membrane potential (−50 mV) in a recorded OT neuron show a time- and voltage-dependent inward rectification and a rebound depolarization caused by the deactivation and reactivation, respectively, of a sustained outward rectification (SOR, modified from Stern and Armstrong 1995). (**b**) Voltage responses in the model MNC to a similar current injection protocol. In all compartments, $g_{NA,i}$ was set to zero in order to prevent action potential firing. (**c**) Steady-state current-voltage characteristics plotted at the end of the hyperpolarizing pulse (*arrows in* (***a***) *and* (***b***)) in the recorded MNC (*open circles, dotted line*) and in the model MNC (*filled circles, solid line*). The currents were normalized to maximal current, which produced a hyperpolarization to −103 mV. (**d**) When sodium conductances ($g_{NA,i}$) were set to their standard values (Table 1), the rebound depolarization following a hyperpolarizing pulse evoked action potentials in the model, which was similar to the response seen in the recorded OT neuron (*a*)

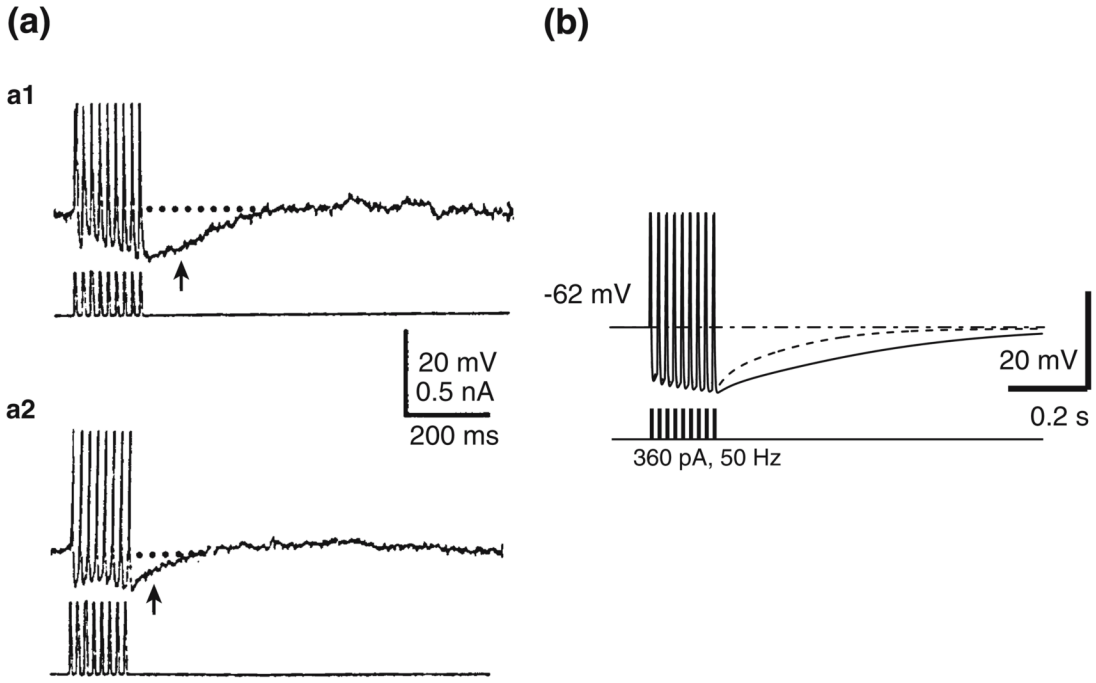

Fig. 10.

Effect of SOR on the AHP. AHPs were evoked in a real MNC (Modified from Armstrong et al. 1994) and in the model MNC by nine current pulses at 50 Hz. (**a**) AHPs (*arrows*) in a VP neuron (*a1*) and in an OT neuron (*a2*) recorded in a slice and identified by immunohistochemistry (Armstrong et al. 1994). (**b**) AHPs generated in the model MNC with I_{SOR} (*dashed line*, τ_{AHP}=188 ms) and without I_{SOR} (*solid line*, τ_{AHP}=424 ms). Spikes are truncated

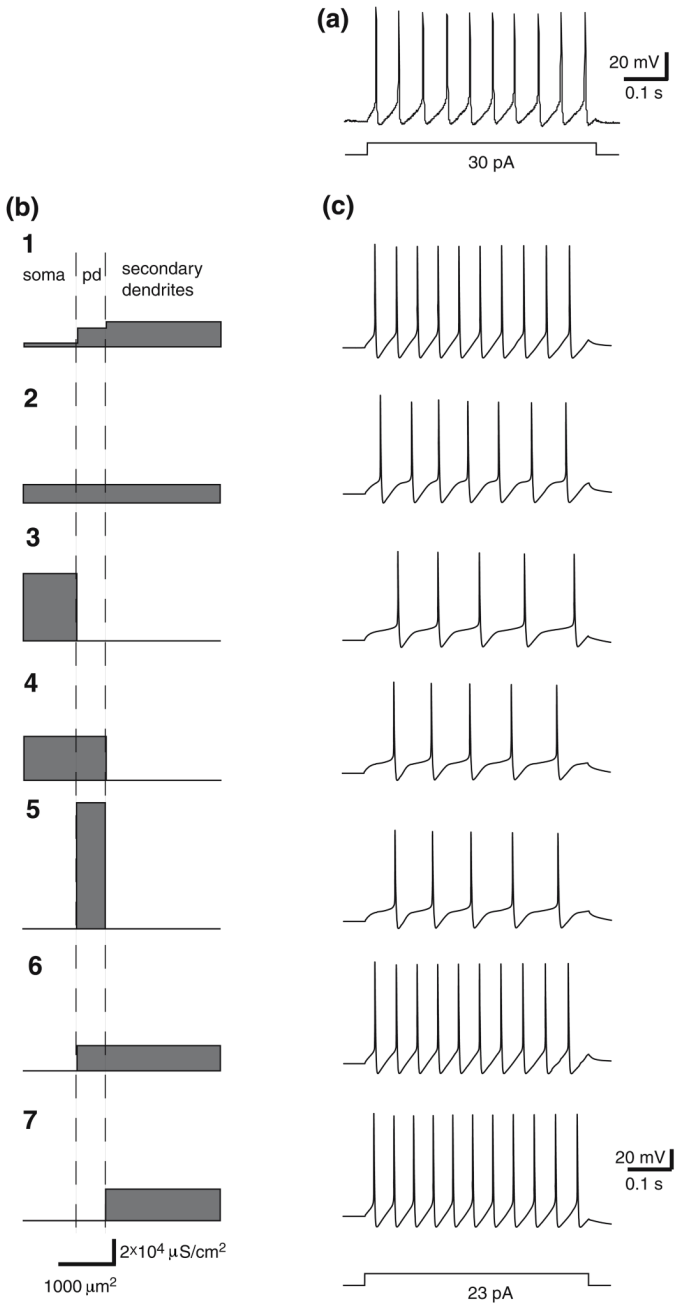

Fig. 11.

Influence of spatial distribution of A-type channels on spiking activity in the model MNC. (**a**) Spike discharge evoked by a 30 pA, 500 ms current pulse in a hypothalamic slice recording of a rat SON MNC (see Boudaba et al. 2003). (**b**) Diagrams showing the relative distributions of g_A in the soma, primary dendrites (pd) and secondary dendrites tested in the model MNC. (**c**) Spike discharges evoked by 500 ms, 23 pA current pulses in the model under the different distributions of g_A shown in *b*. The distributions of *gA* shown in *b1*,*6* and *7* produce repetitive spiking activity in the model that most closely resembles that of MNCs recorded in vitro. The distribution used in the model MNC is that shown in *b1*

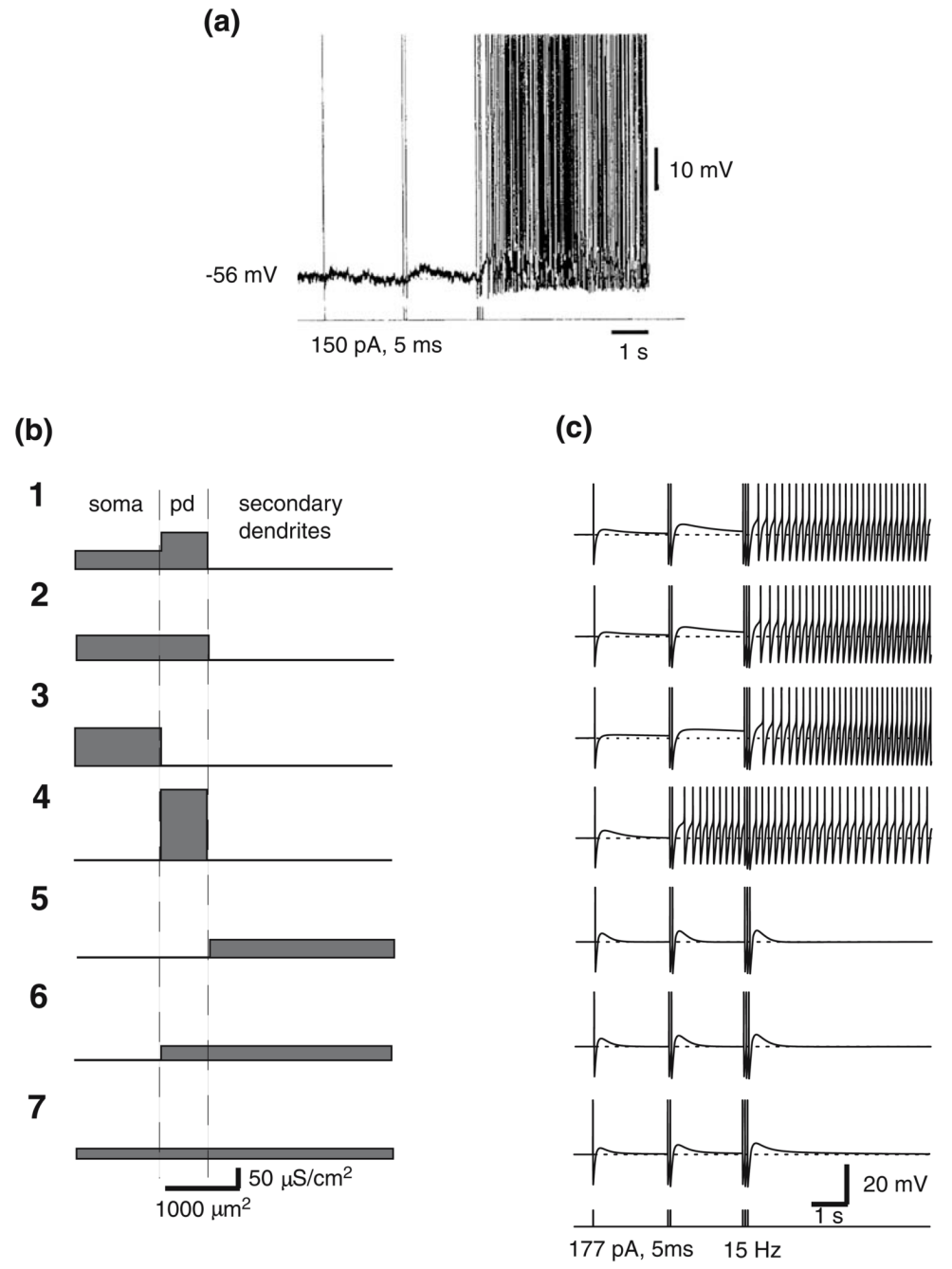

Fig. 12.

Influence of spatial distribution of CAN channels on the DAP. (**a**) Voltage record (*top trace*) from a real MNC demonstrating progressively larger, longer-lasting DAPs and a spike after discharge following an increasing number of spikes (1, 2 and 4) evoked by current injections (*bottom trace*) (modified from Li and Hatton 1997a). (**b**) Diagrams showing the relative distributions of g_{CAN} in the soma, primary dendrites (pd) and secondary dendrites tested in the model MNC. (**c**) DAPs and spike after discharges elicited in the model, with the different distributions of I_{CAN} shown in (**b**), by sequentially increasing the number of current-evoked spikes (1, 2 and 4) according to the stimulation protocol shown below; DAP amplitudes and

durations increased with the number of repetitive conditioning spikes. The distribution used in the model is shown in *b1*. Spikes in (**c**) are truncated

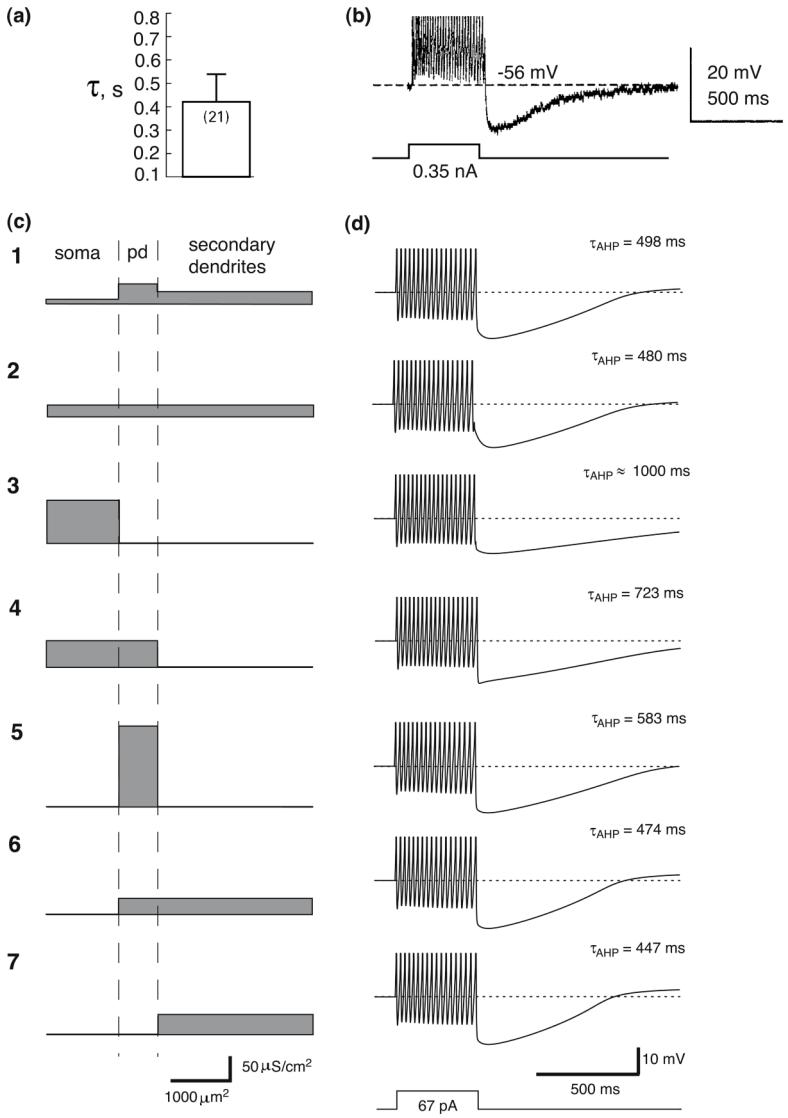

Fig. 13.

Influence of spatial distribution of SK channels on AHPs. (**a**) The time constant of decay of the AHP in VP neurons recorded in a slice (modified from Teruyama and Armstrong 2002). (**b**) Voltage record from a recorded VP neuron showing an AHP following a current-evoked train of action potentials (modified from Teruyama and Armstrong 2002). (**c**) Diagrams showing the relative distributions of g_{SK} in the soma, primary dendrites (pd) and secondary dendrites tested in the model MNC. (**d**) Spike trains and AHPs in the model evoked by 400 ms depolarizing current pulses obtained with the distributions of g_{SK} shown in (**c**). The distributions of SK shown in *c1*, *2*, *6* and *7* from the model produced a waveform and decay time constant of the AHP that most closely resemble those of AHPs recorded in VP neurons *in vitro*. The compartmental distribution of SK used in the model is shown in *c1*. *Dotted lines* indicate −56 mV

Table 1

Standard model parameters (unless otherwise specified)

Parameter	Value	Parameter	Value
d_s	15 μm		
d_{pd}	2 μm	$g_{Ka,i}$	4,000 μS/cm^2
d_{sd}	1 μm	$g_{A,pd}$	15,000 μS/cm^2
L_s	25 μm	$g_{A,sd}$	20,000 μS/cm^2
L_{pd}	50 μm	$g_{SK,s}$	10 μS/cm^2
L_{sd}	200 μm	$g_{SK,pd}$	20–40 μS/cm^2[b]
R_a	200 Ω cm[a]	$g_{SK,sd}$	5–25 μS/cm^2[b]
C_m	1 μF/cm^2	$K_{m,SK}$	0.00033 mM
$g_{Na,s}$	70000 μS/cm^2	$g_{BK,s}$	3,500 μS/cm^2
$g_{Na,pd}$	50000 μS/cm^2	$g_{BK,pd}$	3,000 μS/cm^2
$g_{Na,sd}$	10000 μS/cm^2	$f_{Ca,BK,s}$	0.02
E_{Na}	55 mV	$f_{Ca,BK,pd}$	0.03
$g_{Ca,L,s}$	400 μS/cm^2	r_s	0.015936
$g_{Ca,L,pd}$	220 μS/cm^2	r_{pd}	0.0591
$g_{Ca,L,sd}$	460 μS/cm^2	$K_{BK,s}$	6 ms^{-1}
τ_{mL}	0.9 ms	$K_{BK,pd}$	6 ms^{-1}
$K_{m,L1}$	0.0001 mM	E_K	−100 mV
$K_{m,L2}$	0.002 mM	$g_{CAN,s}$	15–45 μS/cm^2[b]
$g_{Ca,N,s}$	260 μS/cm^2	$g_{CAN,pd}$	30–90 μS/cm^2[b]
$g_{Ca,N,pd}$	100 μS/cm^2	$K_{m,CAN}$	0.0003 mM
τ_{mN}	2.0 ms	a_1	0.000130 mM
$[Ca^{2+}]_o$	2.4 mM	b_1	0.000005 mM
$[Ca^{2+}]_{rest}$	0.00013 mM	a_2	0.000135 mM
$f_{Ca,s}$	0.00714	b_2	0.000070 mM
$f_{Ca,pd}$	0.0035	$V_{CAN,h}$	−10 mV
$f_{Ca,sd}$	0.002	$g_{L,K,i}$	12.5 μS/cm^2
$U_{s,s}$	0.068 ms^{-1}	$g_{L,Na,i}$	5 μS/cm^2
$U_{s,pd}$	0.32 ms^{-1}	$\tau_{m,SOR}$	350 ms^{-1}
$U_{s,sd}$	0.8 ms^{-1}	$g_{SOR,i}$	20 μS/cm^2

[a] Mainen and Sejnowski 1999;

[b] Parameter ranges reproducing MNC activity in different simulated experiments.